

Review

Tuning Redox Transitions via Inductive Effect in Metal Oxides and Complexes, and Implications in Oxygen Electrocatalysis

Denis A. Kuznetsov,^{1,2,6} Binghong Han,^{1,3,6} Yang Yu,^{1,3,6} Reshma R. Rao,^{1,4} Jonathan Hwang,^{1,3} Yuryi Román-Leshkov,⁵ and Yang Shao-Horn^{1,2,3,4,*}

The reduction and oxidation (redox) of transition metals allow storing charge/energy in Li-ion batteries and electrochemical capacitors and play an important role in catalysis of electrochemical reactions, such as oxygen reduction reaction (ORR) in fuel cells and metal-air batteries and oxygen evolution reaction (OER) in electrolytic cells. In this review, we present and discuss a universal origin of inductive effect associated with metal substitution in Ni, Co, Fe, Mn-based complexes, (hydr-)oxides, and lithium intercalation compounds by alignment of the electron levels of metal complex redox with partially filled metal d-state and oxygen p-state of oxides on the absolute energy scale. Increased redox potentials of metal complexes and oxides are shown to correlate with the increased electronegativity of the substituting metal, which results in the enhancement of the ORR/OER activity. Such observations provide new insights into potential strategies to optimize ORR/OER catalytic activity by tuning the redox properties of metal sites.

Introduction

Earth-abundant transition metal oxides are used extensively for storing charge in energy storage devices including Li-ion¹ or Na-ion batteries^{2,3} and electrochemical capacitors,^{4,5} as well as for catalyzing key reactions involved in the chemical transformation of sustainable chemicals and fuels such as oxygen reduction reaction (ORR)^{6,7} and oxygen evolution reaction (OER)^{6,8,9} in fuel cells,¹⁰ electrolytic cells,¹¹ metal-air batteries,¹² and devices for solar fuels.^{13,14} In all of these applications, the reduction/oxidation (redox) of transition metal ions plays a critical role. For example, in Li-ion or Na-ion batteries, the charge/discharge (i.e., Li^+/Na^+ de-intercalation/intercalation) process is accompanied by the redox of transition metal ions in bulk.^{1,3} On the other hand, in fuel cells or electrolytic cells, catalysis of ORR/OER involves the redox of transition metal oxides on or near the surface.^{6,15} Understanding the redox processes in metal oxides could provide a powerful tool for controlling the potentials at which charge/energy can be stored in batteries as well as their capacities, and for enhancing the efficiency of the energy conversion devices by improving the activity of OER/ORR catalysts. One effective way to adjust the redox process in transition metal oxides is through the substitution of metal ions, which is also a common strategy used to tune Li^+/Na^+ intercalation voltages^{16–18} and to increase the OER/ORR catalytic activity.^{15,19–26} However, a universal and fundamental understanding of the foreign metal substitution effect to the redox process across these different applications is still missing.

Context & Scale

This review aims to bridge the fields of inorganic molecular chemistry, electrocatalysis, lithium-ion batteries, and chemical physics of oxides by introducing a unifying concept linking the electronic structures and electrochemical properties of transition metal oxides and complexes. In this work, by reviewing broad literature on the redox behavior of a number of Ni, Co, Fe, and Mn (hydr-)oxides, Li-intercalation compounds, and organometallic complexes, we demonstrate the effect of the foreign metal substitution on their redox potentials and rationalize the trends by aligning the redox couples of metal complexes with the metal d and oxygen p bands of metal oxides on the absolute electron energy scale. The higher Lewis acidity of the metal substituent compared with parent metal leads to the anodic shift of the redox transition potential due to the inductive effect, which is also shown to correlate with oxygen reduction and evolution activity. This study opens up a new perspective for the design of transition metal compounds with tunable redox properties in order to control the thermodynamics and kinetics of the key



In this review, we bridge the studies of redox processes associated with metal substitutions in the fields of inorganic molecular chemistry and Li-ion battery materials, which are reasonably understood, with those in electrocatalysis via the chemical physics of metal complexes and oxides by introducing a unifying concept of electronic levels on the absolute energy scale. Redox processes in transition metal oxides can be probed by electrochemical measurements, synchrotron X-ray absorption spectroscopy (XAS),^{26,27} Raman spectroscopy,^{28,29} electron energy loss spectroscopy (EELS),³⁰ X-ray photoelectron spectroscopy (XPS),^{31,32} and density functional theory (DFT) studies.^{33–35} Among these techniques, electrochemical methods such as cyclic voltammetry (CV) and galvanostatic measurements are simple but informative *in situ* methods providing the thermodynamic and kinetic information about redox processes in transition metal complexes and oxides.

In this work, we show that measuring the redox potential of metal complexes and oxides can be a powerful approach to reveal the inductive effect associated with metal substitution, and to guide the design of metal complexes and oxides for electrochemical energy storage and conversion applications. In the next section (Inductive Effect in Metal Complex and Metal Oxides), we discuss that the inductive effect associated with metal substitution can be used as a universal concept to rationalize and predict the redox potential changes reported in metal complexes,^{36,37} metal (hydr-)oxides,^{19,38} and lithium intercalation oxides^{39–41} by altering the energy levels associated with filled antibonding states of metal-oxygen bonds. The third section (Inductive Tuning of Redox Potentials) demonstrates that substitution with metal ions possessing higher electronegativity in transition metal complexes and oxides correlates with increased thermodynamic redox potentials, which is accompanied by more electron density drawn away from parent metal and the formation of less covalent bonds between parent metal and ligand. In the section titled Implications of Redox Potential Tuning for ORR and OER Kinetics, we show and discuss examples that positive shift of redox potentials in transition metal complexes and oxides caused by the inductive effect can lead to enhanced ORR/OER activity, which can be attributed to reduced adsorption strength of oxygenated species (since they are mostly on the ascending portion of OER/ORR volcano, where weaker surface adsorption leads to higher activity⁴²). Such tuning of redox potential and ORR/OER activity by the inductive effect not only provides new insights into reaction mechanisms on metal oxides, but also represents a conceptually new strategy for materials engineering and opens new avenues for experimental and computational studies devoted to the development of new materials.

Inductive Effect in Metal Complex and Metal Oxides

The inductive effect is defined by the International Union of Pure and Applied Chemistry (IUPAC) as “transmission of charge through a chain of atoms by electrostatic induction,”⁴³ and was introduced into the field of organic chemistry in the 1960s to explain the polarization of molecules upon introduction of substituents into hydrocarbon chain.^{44,45} The inductive effect is also used by Goodenough et al. in the 1990s to rationalize the influence of anions on the lithium intercalation voltage of lithium transition metal compounds^{46–49} such as LiMPO_4 and $\text{Li}_3\text{M}_2(\text{XO}_4)_3$ (having $\text{X} = \text{P, S, Mo, and As}$). High covalency of X-O bond in lithium metal phosphates can lower the covalency of neighboring M-O bond through the inductive effect, which would lower the electron energy of filled antibonding states and increase lithium intercalation voltage relative to lithium metal oxides with nominally identical metal redox couples.^{46–49} For instance, upon replacement of phosphorous with more electronegative sulfur in $\text{Li}_3\text{Fe}_2(\text{PO}_4)_3$, the effective charge of M increases (lowering M-O covalency) as sulfur would withdraw more electron density in X-O-M ,

electrochemical reactions in energy transformation and storage devices, such as electrolyzers, metal-air and metal ion batteries, fuel cells, and supercapacitors.

¹Electrochemical Energy Laboratory

²Research Laboratory of Electronics

³Department of Materials Science and Engineering

⁴Department of Mechanical Engineering

⁵Department of Chemical Engineering

Massachusetts Institute of Technology, 77 Massachusetts Avenue, Cambridge, MA 02139, USA

⁶These authors contributed equally

*Correspondence: shaohorn@mit.edu

<https://doi.org/10.1016/j.joule.2017.11.014>

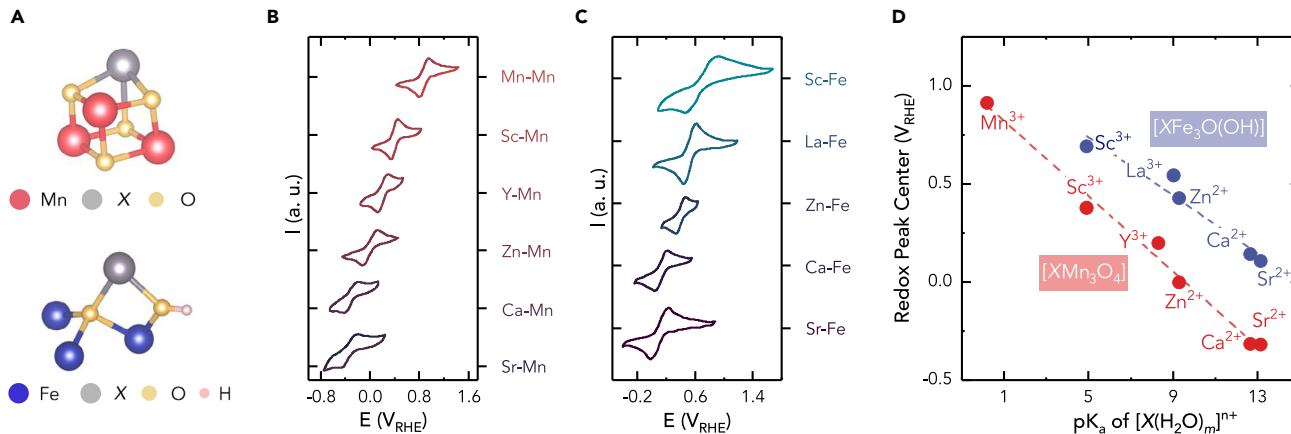


Figure 1. Inductive Effect in Bimetallic Complexes

(A) Schematic representation of $[M\text{-Mn}_3]$ and $[M\text{-Fe}_3]$ cores in complexes $[LMn_3O_4(OAc)_3(L')_x]^{n+}$ ³⁶ and $[LFe_3O(OH)(OTf)_y(L')_z]^{m+}$ ³⁷ ($H_3L = 1,3,5\text{-tris}(2\text{-di(2-pyridyl)}\text{hydroxymethyl)phenyl)benzene}; L' = solvent$).

(B) Cyclic voltammetry curves for $[XMn_3O_4]$ -containing complexes ($X^{n+} = Sr^{2+}, Ca^{2+}, Zn^{2+}, Y^{3+}, Sc^{3+}, Mn^{3+}$). Redox transitions on CV curves correspond to $[XMn^{+4}_2Mn^{+3}O_4]/[XMn^{+4}_3O_4]$ couples.³⁶ The measurements were made in 0.1 M NBu_4PF_6 in a DMA solution with a scan rate of 100 mV/s.³⁶

(C) Cyclic voltammetry curves for $[XFe_3O(OH)]$ -containing complexes ($X^{n+} = Sr^{2+}, Ca^{2+}, Zn^{2+}, La^{3+}, Sc^{3+}$). Redox transitions on CV curves correspond to $[XFe^{+3}_2Fe^{+2}O(OH)]/[XFe^{+3}_3O(OH)]$ couples.³⁷ The measurements were performed in 0.1 M NBu_4PF_6 in a $CH_2Cl_2/1,2\text{-DME}$ (9:1) solution with a scan rate of 200 mV/s.³⁷

Potentials referenced versus the Fc/Fc^+ redox couple were converted to the RHE scale using the equation: $E_{RHE, pH14} = E(Fc/Fc^+) + (0.624 + 0.059 \cdot pH)V$.⁵⁷

(D) Trend between redox transition potentials of $[XMn^{+4}_2Mn^{+3}O_4]/[XMn^{+4}_3O_4]$ ³⁶ in (B) and $[XFe^{+3}_2Fe^{+2}O(OH)]/[XFe^{+3}_3O(OH)]$ ³⁷ in (C) with decreasing pK_a of $[X(H_2O)_m]^{n+}$ ($n = 2$ for Sr, Ca, Zn; $n = 3$ for Y, Sc, Mn).⁵⁸

which is accompanied with an increase in lithium intercalation voltage from 2.8 to 3.6 V versus Li (V_L) corresponding to Fe^{2+}/Fe^{3+} redox couple.⁴⁸ Overall, by affecting the electronic structure, the inductive effect has a direct influence on redox potential of transition metal ions. However, since it can also be affected by other substitution-related factors, such as changes in the morphology and crystal structure,⁵⁰ oxidation state of the parent metal,²⁶ active site,²⁰ and reaction mechanisms,^{15,51} in this review we focus on the previous studies, where the contribution of the effects other than the inductive effect is negligible.

More recently, this inductive effect is manifested in systematic shifts in the redox potential of $[XMn_3O_4]$ -containing and $[XFe_3O(OH)]$ -containing organometallic complexes^{36,37,52,53} (Figure 1A), investigated as a mimic for the $[Mn_4CaO_5]$ active site^{54,55} in the biological oxygen-evolving complex of photosystem II (PSII). In $[XMn_3O_4]$ ³⁶ and $[XFe_3O(OH)]$ ³⁷ metal complex systems, substituents that are more acidic than Ca^{2+} (e.g., $X^{n+} = Zn^{2+}$ or Sc^{3+}) cause a positive shift in the Mn^{3+}/Mn^{4+} and Fe^{2+}/Fe^{3+} redox potential, as shown in Figures 1B and 1C. These potential shifts linearly scale with the pK_a value of $[X(H_2O)_m]^{n+}$ (Figure 1D), where pK_a is equal to $-\log(K_a)$ and K_a is the equilibrium constant for water ligand deprotonation in $[X(H_2O)_m]^{n+} ([X(H_2O)_m]^{n+} = H^+ + [X(H_2O)_{m-1}(OH)]^{(n-1)+})$. Lewis acidity of the hydrated metal cation is essentially a way to define its electronegativity, and represents a direct measure of the strength of inductive effect felt by adjacent atoms: more electronegative cations form more covalent $M\text{-OH}_2$ bonds in $[X(H_2O)_x]^{n+}$ and polarize water O-H bonds more strongly, making them more ionic and more prone to dissociation, or more acidic (decreased pK_a). This trend is further supported by recent computational studies showing that substitution with more acidic ions leads to higher ionization energies.⁵⁶

To facilitate the understanding of the redox potentials observed in the fields of molecular chemistry, electrochemistry, and oxide physics, we examined whether a

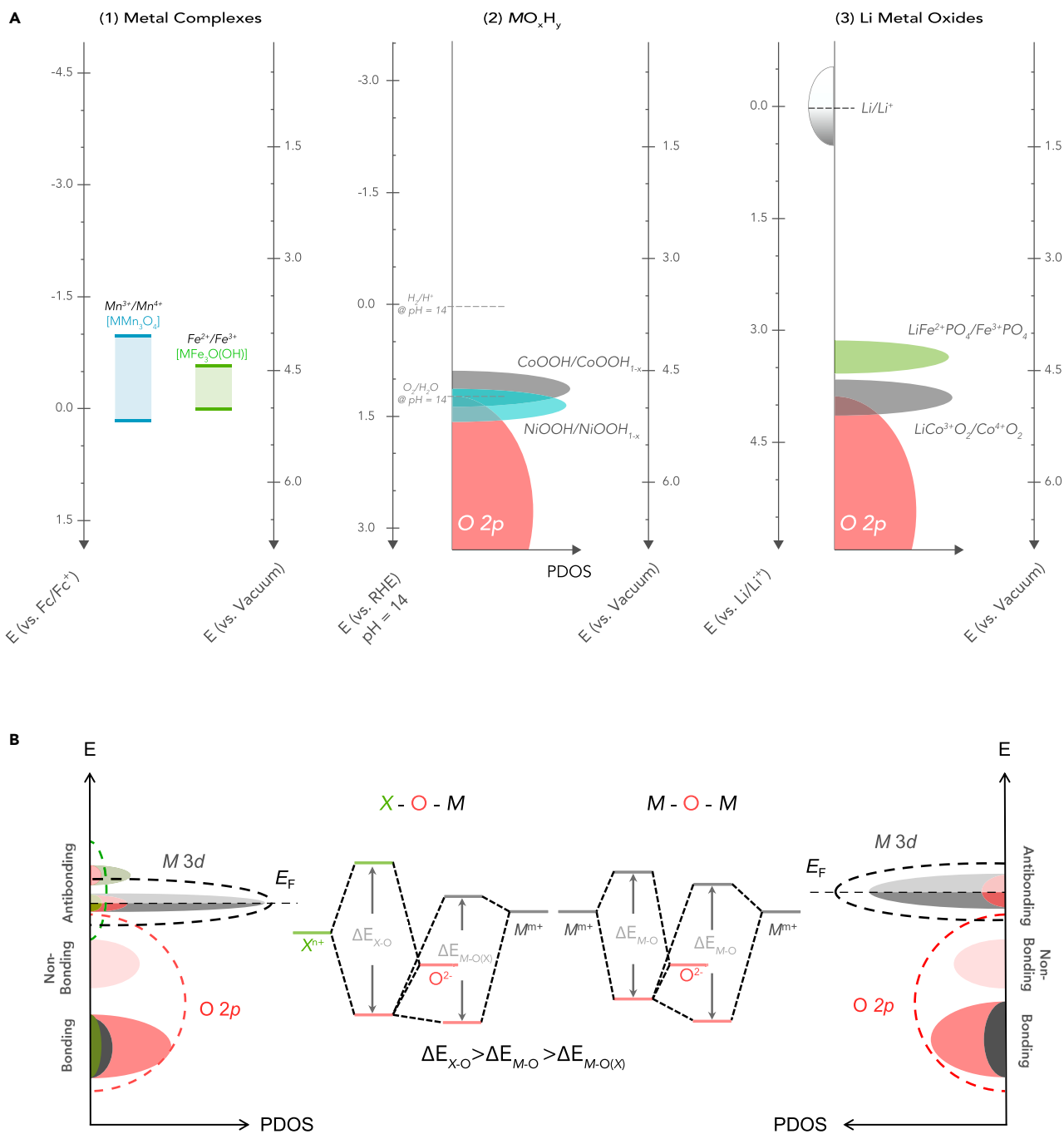


Figure 2. Redox Properties and Electronic Structures of Metal Complexes and (Hydr-)oxides

(A) Alignment of well-known reference scales (reversible hydrogen electrode [RHE, pH 14], ferrocene/ferrocenium [Fc/Fc^+] and Li/Li^+ couples) to the absolute energy scale (versus vacuum) and position of select redox couples. Conversions between scales were performed using equations: E (versus vacuum) = $[E$ (versus RHE, pH = 14) + 4.44 – 0.059 · pH] eV⁶⁵ and E (versus vacuum) = $[E$ (versus Fc/Fc^+) + 0.624 + 4.44] eV⁵⁷. Aligning Li/Li^+ scale with respect to the vacuum was conducted by aligning the redox transition of $\text{LiCo}^{3+}\text{O}_2/\text{Co}^{4+}\text{O}_2$ (~4 V versus Li/Li^+) with the same $\text{Co}^{3+}/\text{Co}^{4+}$ transition in Co (hydr-)oxides (~1.4 V versus RHE, pH 14). This conversion can be approximately expressed by E (versus vacuum) = $[E$ (Li/Li^+) + 1.0] eV. (1) Alignment of the electron energy levels of $\text{Mn}^{3+}/\text{Mn}^{4+}$ redox in $[\text{LXMn}_3\text{O}_4(\text{OAc})_3(\text{X}')_x]^{n+}$ clusters³⁶ and $\text{Fe}^{2+}/\text{Fe}^{3+}$ in $[\text{LXFe}_3\text{O}(\text{OH})(\text{OTf})_y(\text{L}')_z]^{m+}$ clusters³⁷ ($\text{H}_3\text{L}' = 1,3,5\text{-tris}(2\text{-}(2\text{-pyridyl})\text{hydroxymethyl})\text{phenyl}\text{benzene}$, $\text{L}' = \text{solvent}$). (2) Alignment of valence band schematics of oxyhydroxides involving $\text{NiOOH}/\text{NiOOH}_{1-x}$ and $\text{CoOOH}/\text{CoOOH}_{1-x}$. (3) Alignment of valence band schematics of $\text{LiCoO}_2/\text{Li}_{1-x}\text{CoO}_2$ and phosphates with $\text{Fe}^{3+}/\text{Fe}^{2+}$ in LiFePO_4 ($\text{LiCoO}_2 = \text{Li}_{1-x}\text{CoO}_2 + x\text{Li}^+ + xe^-$ ⁶⁶; $\text{LiFePO}_4 = \text{Li}_{1-x}\text{FePO}_4 + x\text{Li}^+ + xe^-$ ⁶⁷).

Figure 2. Continued

(B) Schematics of molecular orbitals of M-O-M and X-O-M (center) and valence bands of $(H, Li)_x MO_y$ and $(H, Li)_x (X, M)O_y$ (left and right, drawing adapted from Pavlishchuk and Addison⁵⁷), where substituent X^{n+} is more electronegative than M^{m+} . The filling of metal antibonding states is arbitrary but kept the same for both scenarios. Discrete bonding, nonbonding, and antibonding states are depicted as solid lines. The nonbonding and antibonding states are also shown as several single broad bands (dashed lines). For more electronegative X^{n+} , forming more covalent bond with oxygen than M^{m+} , the energy separation between antibonding and bonding state (ΔE_{X-O}) is higher than that of M-O bond (ΔE_{M-O}). By substituting X^{n+} , M-O(X) bond gains more ionic character than for the nonsubstituted case, resulting in a smaller energy separation between bonding and antibonding orbitals ($\Delta E_{M-O(X)}$) compared with the unsubstituted case.

common physical origin can be found for oxygen-containing metal complexes and oxides. First we aligned the electrode scales of Fc/Fc^+ (used commonly in electrochemistry of molecular compounds), H_2/H^+ (reversible hydrogen electrode, RHE, used in electrocatalysis), and Li/Li^+ (used in Li-ion battery studies) scales to the absolute electron energy, as shown in Figure 2A. Electrode potentials reported for the redox of select metal complexes referenced to Fc/Fc^+ are aligned with those of select metal (hydr-)oxides explored as catalysts for water splitting^{59,60} and as electrochemical capacitors (referenced to RHE), and of transition metal in lithium-ion intercalating materials for Li-ion batteries (referenced to Li/Li^+).^{49,61} Such alignment allowed us to note that the redox of metal-oxygen-containing complexes (e.g., $Fe^{+3}2Fe^{+2}O(OH) = Fe^{+3}3O(OH) + e^-$,³⁷ hydroxide-mediated deprotonation/protonation in metal oxyhydroxides^{59,60} (e.g., $NiOOH = NiOOH_{1-x} + xH^+ + xe^-$) and lithium de-intercalation/intercalation in metal oxides (e.g., $LiCoO_2 = Li_{1-x}CoO_2 + xLi^+ + xe^-$) could occur in similar electron energy levels. Due to increased hybridization between transition metal and ligand, which can create a ligand hole for late transition metal ions (e.g., Ni^{3+} , Ni^{4+} and Co^{4+}),⁶²⁻⁶⁴ redox of these late transition metal compounds can involve both metal and ligands.

Metal substitution in transition metal complexes and oxides can result in the redistribution of an electronic density between metal and ligand.⁵⁶ The hybridization of the metal (M) d orbitals and ligand such as O $2p$ orbitals occur due to the spatial overlap and energetic similarity of the electronic states, which result in σ -bonding states, with largely oxygen character, and σ^* -antibonding states with largely metal character,⁶⁸ as shown in Figure 2B (center). Some O $2p$ states (lighter pink in Figure 2B, center) do not hybridize with metal d states and thus form nominally nonbonding (σ_0) states. These molecular orbitals become bands in oxide crystals due to the translational symmetry of the unit cell, resulting in an $M d$ band and O $2p$ band, as shown on the left or right side of Figure 2B.

Metal substituents (X^{n+}) with higher affinity to electrons (with higher electronegativity⁶⁹ or stronger Lewis acids) than parent metal (M^{m+}) can pull electrons from M^{m+} and lower the energy of antibonding states, which would lower the electron energy associated with the redox of M-ligand bonds, and shift the electrode potential positively. An electrode potential shift caused by the inductive effect can be as high as ~ 1 V, as shown in Figure 2A. The molecular orbital diagrams of M-O-M and X-O-M are shown in Figure 2B (center), where substituent X^{n+} has higher electronegativity than parent M^{m+} . X^{n+} with higher electronegativity lies lower on the electron energy scale than M^{m+} , which could lead to the formation of more covalent X-O bond, having a larger energy separation between the bonding and antibonding orbitals than M-O. The bonding orbitals of X-O can be further hybridized with M^{m+} in X-O-M to form M-O bonds adjacent to X-O, where antibonding states have lower electron energy, and M-O bonds in X-O-M are less covalent. Forming extended lattice with

these bonds would give rise to narrower d states and lower electron energy for the valence band top edge compared with the nonsubstituted case, as shown in Figure 2B (left and right sides). On the other hand, metal substituents with lower affinity to electron density can donate electrons to parent metal and increase the filling of antibonding states, which would increase the electron energy for redox of parent metal ions and shift the electrode potential negatively.

In this section, we have demonstrated that metal substituents (X^{n+}) with higher affinity to electrons (i.e., with higher electronegativity or stronger Lewis acids) than the parent metal (M^{m+}) can lower the energy of the antibonding states, thus increasing the voltage of the redox transitions. In the following sections, we apply the inductive effect concept established for redox processes in metal complexes and lithium metal oxides to the redox potential changes in Ni, Co, and Fe-based (hydr-)oxides, and complexes used for catalyzing ORR/OER. Implications of redox potential tuning through the inductive effect on the ORR/OER activity are discussed.

Inductive Tuning of Redox Potentials

Ni-Based Oxides

Corrigan and Bendert⁷⁰ have systematically shown that metal substitution such as Ce and Zn in electrodeposited Ni(OH)_2 can promote the OER kinetics. The enhanced OER kinetics is accompanied with a positive shift in the potential of a reversible process for the oxidation of Ni(OH)_2 prior to the onset of OER.⁷⁰ This redox process (centered at ~ 1.4 V versus RHE [V_{RHE}]) and involving 1.6 electrons per Ni(OH)_2) has been attributed to hydroxide-mediated deprotonation/protonation or proton de-intercalation/intercalation from/into Ni(OH)_2 ,⁷⁰ involving $\text{Ni(OH)}_2 + \text{OH}^- \rightarrow \text{NiOOH} + \text{H}_2\text{O} + \text{e}^-$ and $\text{NiOOH} + x\text{OH}^- \rightarrow \text{NiO}_{1+x}\text{(OH)}_{1-x} + x\text{H}_2\text{O} + x\text{e}^-$ processes.^{71–73} Although some studies^{74–81} have assigned this peak as the $\text{Ni}^{2+}/\text{Ni}^{3+}$ redox between $\text{Ni}^{2+}\text{(OH)}_2$ and Ni^{3+}OOH , there is compelling evidence to support the involvement of nominal Ni^{4+} and oxygen redox accompanied with nominal Ni^{4+} , which is supported by recent X-ray near-edge spectroscopy measurements of bulk Ni oxidation state (reaching $\sim 3.6+$).^{82–85} The participation of oxygen redox associated with nominal $\text{Ni}^{3+}/\text{Ni}^{4+}$ transition can be explained by its electron energy pinned on top of the oxygen p band, which is also supported by severe oxygen loss associated with Li-ion battery material $\text{Li}_x\text{Ni}^{3+}\text{O}_2$ upon lithium de-intercalation.⁸⁶ The role of metal substitution on the shift of the redox process centered at ~ 1.4 V_{RHE}⁷⁰ and the OER kinetics is further confirmed by recent comprehensive studies from Boettcher et al.¹⁹ For example, the redox peak center was found to shift positively with metal substitution in an increasing order from La^{3+} , Ce^{3+} , Ti^{4+} , and Fe^{3+} , as shown in the CV data in Figure 3C. Although it has been proposed that metal substitution-induced shifts in the redox potential centered at ~ 1.4 V_{RHE} may arise from an electronic structure change,⁷⁰ details are not known to date.

Here we employ the inductive effect concept illustrated in Figure 2B to explain the shift in the redox potential previously observed for metal-substituted Ni(OH)_2 .^{19,70} We found that the redox weighted center position extracted from Figure 3C, representing the formal potential, shifted positively with greater electron withdrawing strength of substituting ions (X^{n+}) manifested in increased electronegativity of X^{n+} ⁸⁸ (Figure 3E-1). Greater electronegativity of substituting metal ions can lower $\text{Ni}^{3+/4+}-\text{O}$ bond covalency (Figure 2B), which would lead to lowering of the electron energy for the top of the valence band and increase the potential for the proton-coupled electron transfer relative to RHE scale. Moreover, the redox peak center shifts positively with decreasing pK_a (increased Lewis acidity) of corresponding

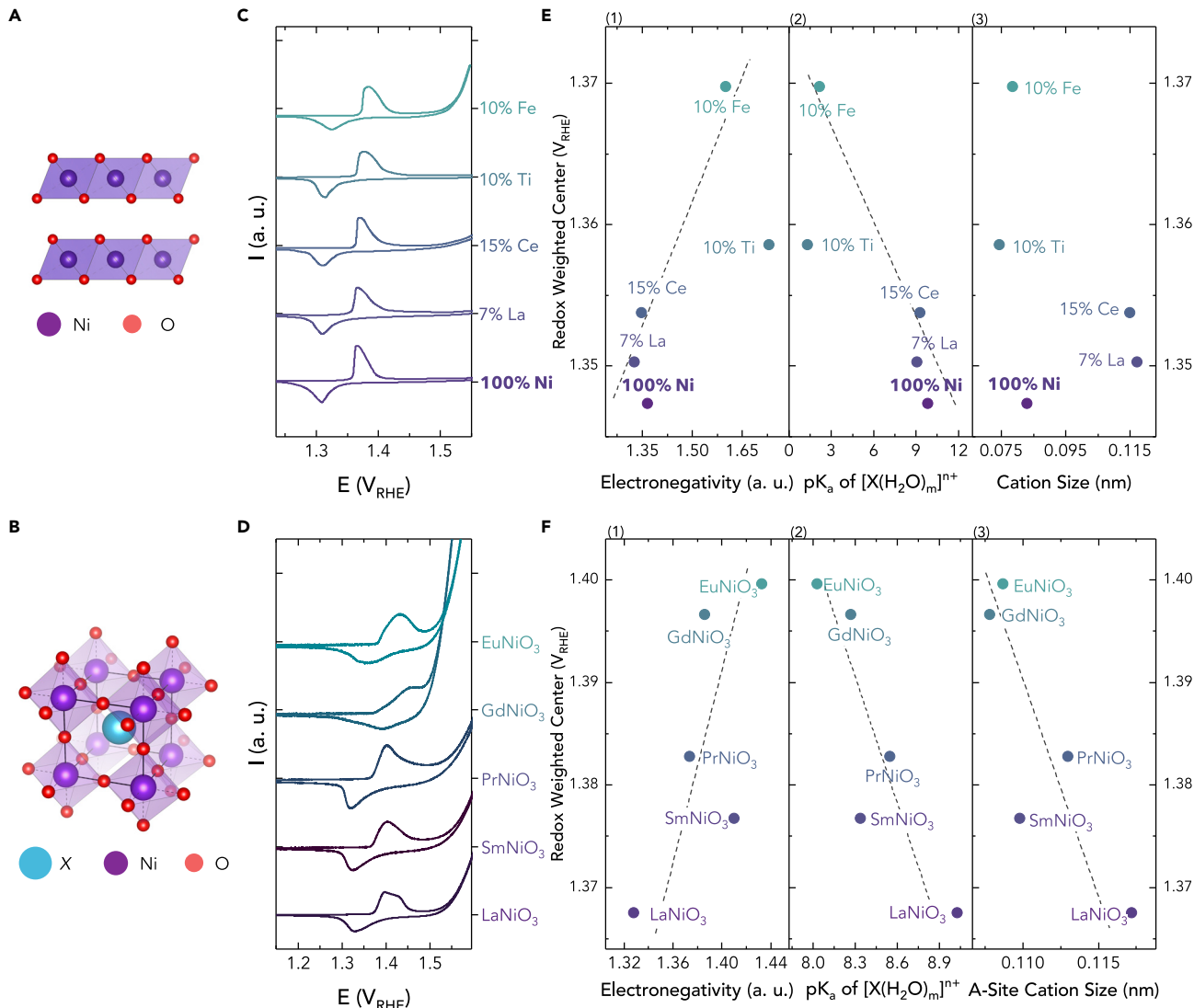


Figure 3. Inductive Effect in Ni-Based (Hydr-)oxides

(A and B) Representations of the crystal structure of (A) layered $\text{Ni}(\text{OH})_2$ and (B) XNiO_3 perovskites.

(C) Selected CV curves of spin-cast nickel hydroxide substituted by transition metal ions taken from previous work.¹⁹ The curves were measured in O_2 -saturated 1 M KOH with a scan rate of 20 mV/s.

(D) Selected CV curves of XNiO_3 perovskite oxides measured in O_2 -saturated 0.1 M KOH, with a scan rate of 10 mV/s.

(E) The relationship between the weighted center position of the Ni redox peaks in (C) and the (1) electronegativity, (2) pK_a of $[\text{X}(\text{H}_2\text{O})_m]^{n+}$, (3) X^{n+} cation size, and of the substituting X^{n+} ions in $\text{Ni}_{1-x}\text{X}_x\text{O}_y\text{H}_z$, where $\text{X}^{n+} = \text{La}^{3+}, \text{Ce}^{3+}, \text{Fe}^{3+}$, and Ti^{4+} (the substituent X^{n+} concentration noted next to each data symbol). The process of extracting redox-weighted potential is schematically depicted in Figures S1 and S3.

(F) The relationship between the weighted center position of the redox peaks in (D) and the (1) electronegativity, (2) pK_a of $[\text{X}(\text{H}_2\text{O})_m]^{n+}$, and (3) cation size of the A-site ion in XNiO_3 perovskites, where the A-site ion $\text{X}^{n+} = \text{La}^{3+}, \text{Sm}^{3+}, \text{Pr}^{3+}, \text{Gd}^{3+}$, and Eu^{3+} . The process of extracting redox-weighted potential is described in Figures S2 and S3. Dashed lines represent the linear fitting of the data. In (E) and (F), the values of pK_a for $[\text{Ni}(\text{H}_2\text{O})_x]^{2+}$, $[\text{La}(\text{H}_2\text{O})_x]^{3+}$, $[\text{Ce}(\text{H}_2\text{O})_x]^{3+}$, $[\text{Fe}(\text{H}_2\text{O})_x]^{3+}$, $[\text{Ti}(\text{H}_2\text{O})_x]^{4+}$, $[\text{Sm}(\text{H}_2\text{O})_x]^{3+}$, $[\text{Pr}(\text{H}_2\text{O})_x]^{3+}$, $[\text{Gd}(\text{H}_2\text{O})_x]^{3+}$, and $[\text{Eu}(\text{H}_2\text{O})_x]^{3+}$ were taken from previous work.⁸⁷ The electronegativity values were taken from previous work.⁸⁸

hydrated ions $[\text{X}(\text{H}_2\text{O})_m]^{n+}$ ⁸⁷ in Figure 3E-2, which is similar to the trends discussed previously for the redox of metal complexes (Figure 1D). The oxidation states of substituting metal ions ($\text{La}^{3+}, \text{Ce}^{3+}, \text{Fe}^{3+}, \text{Ti}^{4+}$) used in Figure 3E were chosen based on the oxidation states of precursors used for the synthesis of metal-substituted nickel hydroxide (due to uncertainty about the oxidation state of Mn in a film, this data point was excluded from analysis).

Similar correlations were observed for $X\text{NiO}_{3-\delta}$ perovskites (Figure 3D) known to be highly active for OER.⁸⁹ A redox process centered at $\sim 1.4 \text{ V}_{\text{RHE}}$ was observed for $X\text{NiO}_3$ similar to Ni(OH)_2 , which can be attributed to hydroxide-mediated oxidation/deprotonation of X-substituted Ni(OH)_2 associated with the surface transformation of $X\text{NiO}_3$ at OER potentials. This hypothesis is supported by previous studies of $(\text{Ba},\text{Sr})(\text{Co},\text{Fe})\text{O}_{3-d}$ (BSCF) perovskites with O p-band center similar to that of $X\text{NiO}_3$,⁹⁰ which can transform into layered oxyhydroxides at OER potentials.^{91,92} Previous studies^{91,92} have shown that oxides with O 2p band center too close to the Fermi level (those possessing higher intrinsic activity) may have its surface layer degraded during OER process. Moreover, there is a general trend between catalyst activity and its stability⁹³ predicting low surface stability for more intrinsically active materials. It should be noted that distinguishable redox peaks were not observed in XMnO_{3-d} ,⁹⁴ XFeO_{3-d} ,^{91,94,95} or XCoO_{3-d} ^{15,91} ($X = \text{La}$ and/or Sr) with lower O p-band centers than BSCF. For these systems, due to the larger distance between Fermi level and O p band, the surfaces of these oxides in the electrolyte remain crystalline and have low oxygen vacancy, without transformation to layered oxyhydroxides up to OER potentials, and therefore with no detectable redox peaks observed from CV. Remarkably, the redox peak potential was found to shift positively with increasing electronegativity of X^{n+} (Figure 3F-1), decreasing pK_a of $[X(\text{H}_2\text{O})_m]^{n+}$ (Figure 3F-2) and X ionic size (Figure 3F-3) in the order $\text{La} < \text{Sm} < \text{Pr} < \text{Gd} < \text{Eu}$. This trend can be rationalized by the inductive effect with different A-site ions in the perovskite structure, which is supported by slightly reduced oxygen K-edge XAS pre-peak width (ligand hole) from La, Pr, Sm, Eu, to Gd.^{96,97} Notably, the positive redox potential shift with decreased X^{n+} ionic size (Figure 3F-3) most probably originates from the correlations between size and electronegativity in a row of lanthanides: elements with smaller ionic size typically possess higher electronegativity.⁸⁸

Co-Based Oxides

Here we further compare the redox processes observed for Ni-based oxides with those of Co-based oxides. In contrast to Ni-based oxides shown in Figure 3, having one set of redox peak at $\sim 1.4 \text{ V}_{\text{RHE}}$, Co-based oxides and phosphates can exhibit two sets of redox peaks in the voltage range between 1 and $1.6 \text{ V}_{\text{RHE}}$, as shown in Figure 4A. For example, the CV data of layered LiCoO_2 ⁹⁸ (space group $\text{R}\bar{3}\text{m}$) and $\text{Na}_{0.7}\text{CoO}_2$ (space group $\text{P}6_3/\text{mmc}$) exhibit two redox peaks at ~ 1.1 and $\sim 1.4 \text{ V}_{\text{RHE}}$. It is proposed that both redox processes can be attributed to hydroxide-mediated deprotonation/protonation coupled with nominal $\text{Co}^{3+}/\text{Co}^{4+}$ redox in $\text{Co}^{3+}\text{OO(H, Li/Na)}$.^{15,99-101} This assignment is supported by the voltage plateaus of oxygen intercalation into oxygen-deficient perovskites in the voltage range of 1.2–1.4 V_{RHE} , as shown in Figure 4B. These plateaus are associated with oxygen vacancy filling via $\text{SrCoO}_{3-\delta} + 2\delta\text{OH}^- \rightarrow \text{SrCoO}_3 + \delta\text{H}_2\text{O} + 2\delta\text{e}^-$ ^{102,103} driven by the energy difference between the $\text{H}_2\text{O}/\text{O}_2$ redox couple and the Co 3d states near the Fermi level of $\text{SrCoO}_{3-\delta}$ (Figure 2A). Further support for the $\text{Co}^{3+}/\text{Co}^{4+}$ redox at these potentials came from lithium de-intercalation/intercalation into LiCoO_2 ,³⁹⁻⁴¹ which occurs in the range from ~ 4.0 to $\sim 4.5 \text{ V}_{\text{Li/Li}^+}$ corresponding to 1.0 to $1.5 \text{ V}_{\text{RHE}}$ (Figure 1). Unlike LiCoO_2 and $\text{Na}_{0.7}\text{CoO}_2$, LiCoPO_4 , CoOOH ³⁸ and Fe-substituted CoOOH ³⁸ only show one redox peak at $\sim 1.1 \text{ V}_{\text{RHE}}$ (Figure 4A). Lack of structures capable of hydroxide-mediated deprotonation/protonation at $1.4 \text{ V}_{\text{RHE}}$ might be responsible for the difference, which requires further studies.

Although systematic metal substitution was found for CoOOH ,³⁸ data available did not allow the extraction of formal potentials as shown for Ni(OH)_2 in Figure 3. Nevertheless, we found that reversible voltages of lithium de-intercalation/intercalation in

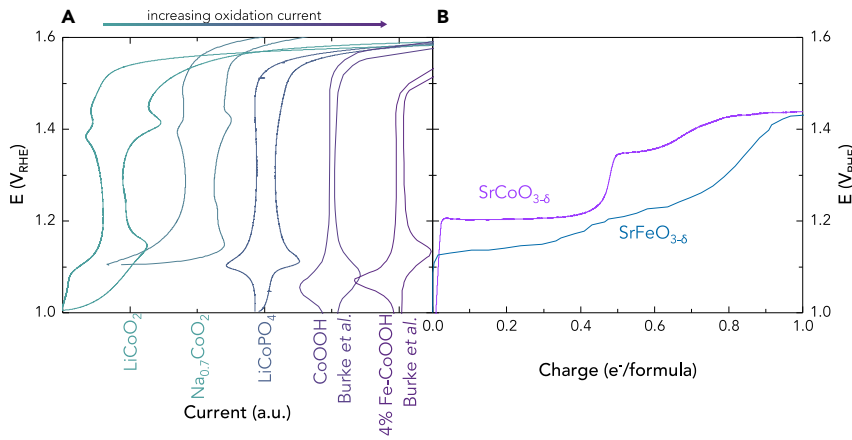


Figure 4. Redox Features of Co-Based (Hydr-)oxides

(A) Selected CV curves of Co-containing compounds measured in O_2 -saturated 0.1 M KOH with a scan rate of 10 mV/s. The data of CoOOH and 14%Fe-CoOOH were taken from previous work,³⁸ which were measured in O_2 -saturated 1 M KOH at a scan rate of 10 mV/s.

(B) Electrochemical oxidation of brownmillerite $SrCo_{3-\delta}$ and $SrFe_{3-\delta}$, where oxygen insertion occurs by $SrMO_{3-\delta} + 2\delta OH^- \rightarrow SrMO_3 + \delta H_2O + 2\delta e^-$ ^{15,102,103} in O_2 -saturated 1 M KOH at a rate of 7.2 and 29.2 mA/g_{oxide}, respectively.

$LiCo_xX_{1-x}O_2$ reported previously could also be tuned by the inductive effect associated with X substitution of Co. The voltages of $LiCo_xX_{1-x}O_2$ were found to increase with increasing electronegativity of X (Figure 5A-1) and with decreasing pK_a of the corresponding substituent (Figure 5A-2), exhibiting similar trends found for substituted $Ni(OH)_2$ in Figure 3. Substituents X such as Mg^{2+} and Zn^{2+} with lower electronegativity compared with Co^{3+} increase the covalency of M-O in X-O-M relative to M-O-M, which raises the electron energy of valence band top edge of $LiCo_{1-x}X_xO_2$ and decreases the electron energy or potential difference relative to Li/Li^+ (or lithium intercalation voltage).

Fe-Based Oxides

Although no systematic studies on the effect of metal substitution were found in the literature for $Fe(OH)_2$ or $FeOOH$, metal substitution in $LiFe_xX_{1-x}PO_4$ ¹⁰⁴ ($X^{n+} = Ni^{2+}$, Mg^{2+} , Al^{3+} , V^{3+}) led to similar trends in the lithium de-intercalation/intercalation voltage as a function of X^{n+} electronegativity and pK_a of $[X(H_2O)_m]^{n+}$. Lithium de-intercalation/intercalation associated with the $LiFe^{2+}PO_4/Fe^{3+}PO_4$ redox occurs at 3.5 V_{Li/Li⁺},¹⁰⁵ which compares well with the potentials of Fe^{2+}/Fe^{3+} redox in Fe-based complexes discussed in Figure 1 (e.g., ~1.0 V_{RHE-pH14} or ~3.9 V_{Li/Li⁺} for $[CaFe^{+3}_3O(OH)]$ and $[SrFe^{+3}_3O(OH)]$) and the potential of oxygen insertion in $SrFeO_{3-\delta}$ shown in Figure 4B (~1.1 V_{RHE-pH14} or ~4.0 V_{Li/Li⁺}). Substituting Fe with ions with higher electronegativity (Figure 5B-1) or lower pK_a of $[X(H_2O)_m]^{n+}$ (Figure 5B-2) leads to increased intercalation voltages. Such trends can be explained by the inductive effect, whereby substitution of Fe^{2+} with X^{n+} characterized with higher electronegativity lowers Fe-O covalency for X-O-Fe bonds, and increases lithium de-intercalation/intercalation voltage for $LiFe_xX_{1-x}PO_4$.¹⁰⁴ However, we should note that in the case of a small difference in electronegativity, the inductive effect can be outweighed by the lattice parameters, intercalation kinetics, and phase miscibility. MuraliGanth et al.⁵⁰ have reported that by substitution of Fe^{2+} by less electronegative Mn^{2+} in the $LiFePO_4$ system, the Li-intercalation voltage is actually increased, which can be attributed to the significantly larger ionic radius of Mn^{2+} that causes stretching of the Fe-O bond, thus decreasing its covalency.

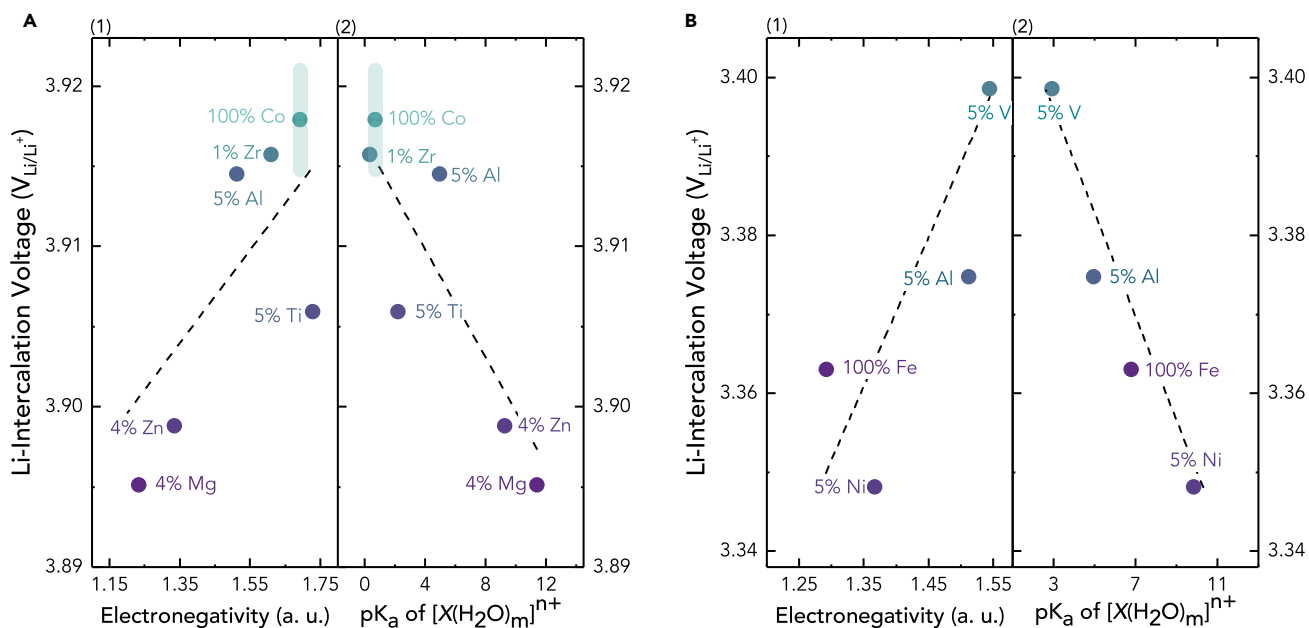


Figure 5. Inductive Effect in Lithium Intercalation Compounds

(A) The relationship between averaged charge and discharge plateau of substituted lithium metal oxides $LiCo_xX_{1-x}O_2$ ($X^{n+} = Ti^{4+}, Mg^{2+}, Al^{3+}, Zn^{2+}, Zr^{4+}$) and the (1) electronegativity and (2) pK_a of $[X(H_2O)_m]^{n+}$ of the substituent X^{n+} . The plateau voltages were extracted from previous work^{39–41} using the methods described in Methodology and Measurements shown schematically in Figure S4. The raw data used for the analysis are shown in Figure S5. The concentration of substituent is indicated next to each individual data point. The electronegativity values were taken from previous work,⁸⁸ and the values of pK_a for $[Ni(H_2O)_m]^{2+}$, $[Mg(H_2O)_m]^{2+}$, $[Al(H_2O)_m]^{3+}$, $[V(H_2O)_m]^{3+}$, $[Ti(H_2O)_m]^{4+}$, $[Zn(H_2O)_m]^{2+}$, and $[Zr(H_2O)_m]^{4+}$ were taken from Dean.⁸⁷

(B) The relationship between discharge plateau of metal-substituted olivines $LiFe_xX_{1-x}PO_4$ ($X^{n+} = Ni^{2+}, Al^{3+}, V^{3+}$) and the pK_a of $[X(H_2O)_m]^{n+}$ and electronegativity of the substituent X^{n+} . The voltage plateau positions were extracted from previous work,¹⁰⁴ using the methods described in Methodology and Measurements shown schematically in Figure S4. The raw data used for the analysis are shown in Figure S5. For all data points, the position of the voltage plateau was estimated as an onset of the lithium de-intercalation/intercalation current.

They have also pointed out that the inductive effect is also violated by substituting Mg^{2+} , which might be attributed to single-phase reaction behavior in contrast to the two-phase reaction behavior in other substituted systems.^{50,51}

From the above discussion, it follows that the electrochemical measurement of metal redox potentials is an effective way to reveal and quantify the influence of the inductive effect on electronic structures of metal centers in metal-substituted Ni-, Co-, and Fe-based (hydr-)oxides. In the following section, we show that the redox potential shifts that originated from the inductive effect can also be used to predict and tune the ORR and OER kinetics on the corresponding metal-substituted (hydr-)oxides.

Implications of Redox Potential Tuning for ORR and OER Kinetics

Here we discuss that tuning the potential of redox events adjacent to ORR/OER can be used to enhance ORR/OER activity of catalysts. Conventional ORR and OER mechanism on oxides from previous experimental and computational studies involves four consecutive proton-coupled electron transfer steps occurring on single metal sites^{27,106–108} or adjacent metal sites.^{34,100} In the case of ORR/OER in basic solution, molecular oxygen or OH^- from the electrolyte and electron interact with surface metal sites to create four different oxygenated adsorbates such as O_2 , OOH , O , and OH , where surface M sites can be oxidized or reduced (formal oxidation state of the metal switches between $n+$ and $n+1$), as shown in Figure 7A for ORR and in Figure 8A for OER. The pioneering DFT works by Nørskov et al.^{107,109–111} had

established a universal framework for ORR/OER kinetics on metal and metal oxide surfaces. As the binding energies of different reaction intermediate species are correlated,^{112,113} the ORR/OER activity can be described by the probability to overcome the largest thermodynamic barrier associated with the rate-limiting step. In the conventional mechanism, the ORR/OER activity of metal oxides scales with the free energy of adsorbates such as ΔG_{Oad} ¹⁰⁶ or $\Delta G_{\text{Oad}} - \Delta G_{\text{OHad}}$ ¹⁰⁷ (referred to as activity descriptor), exhibiting a volcano shape,^{106,107,112} with highest activity corresponding to the intermediate binding strength of the reaction intermediates. Unfortunately, the free energies of adsorption, the key to bridging experimental and computational results of ORR/ORR, are difficult to access experimentally.

The term $\Delta G_{\text{Oad}} - \Delta G_{\text{OHad}}$,¹⁰⁷ introduced as an activity descriptor from DFT studies, is directly related to the redox potentials of metal oxides prior to ORR/OER. For example, the free energy of the proton-coupled electron transfer step, $[\text{M}^{n+}\text{-OH}] \rightarrow [\text{M}^{n+1}\text{-O}] + \text{H}^+ + \text{e}^-$ in acid or $[\text{M}^{n+}\text{-OH}] + \text{OH}^- \rightarrow [\text{M}^{n+1}\text{-O}] + \text{H}_2\text{O} + \text{e}^-$ in basic solution (step n = 3 in Figure 7A and step n = 1 in Figure 8A), can be expressed as $\Delta G = \Delta G_{\text{Oad}} - \Delta G_{\text{OHad}} - eU_{\text{RHE}}$, where ΔG_{Oad} and ΔG_{OHad} are the free energies of adsorption of O_{ad} ($\text{M}^{n+1}\text{-O}_{\text{ad}}$) and OH_{ad} ($\text{M}^{n+}\text{-OH}_{\text{ad}}$), respectively.¹⁰⁷ Therefore, the experimentally observed potential of $[\text{M}^{n+}\text{-OH}_{\text{ad}}]/[\text{M}^{n+1}\text{-O}_{\text{ad}}]$ redox couple prior to ORR/OER might relate to the computational activity descriptor: $\Delta G_{\text{Oad}} - \Delta G_{\text{OHad}} = eU_{\text{RHE}}$. Kuo et al.¹¹⁴ have first used this approach to correlate OER activity at different pH with estimated $\Delta G_{\text{Oad}} - \Delta G_{\text{OHad}}$ from the experimental redox potential (~1.5 V_{RHE} at pH 13) measured for the IrO₂ (110) surface. In the section titled OER Activity we will discuss the limitations of this approach caused by difficulties of the assignment of redox transition prior to a catalytic event.

ORR Activity

We seek to correlate the potential of redox transitions of metal oxides with ORR activity due to its simplicity relative to previously reported activity descriptors for ORR. Previous work has shown that the intrinsic activity of oxides can exhibit a volcano trend²⁷ as a function of the antibonding ("e_g") orbital filling^{115–117} of surface transition metal ions, where having antibonding orbital filling of zero/two can lead to too strong/weak binding of reaction intermediates and having "e_g" close to 1 renders optimum binding and high ORR activity. Such an argument is in agreement with computational studies of metal oxides, which show that the maximum ORR activity is to be observed when binding of oxygenated species such as O₂, OOH, O, and OH is neither too strong nor too weak on the surface metal ions.¹⁰⁶ Moreover, increasing metal-oxygen covalency of metal oxides is shown to increase ORR activity for metal oxides with "e_g" filling of ~1.²⁷ Unfortunately these activity descriptors were estimated from previous *ex situ* measurements of "e_g" filling or obtained from computed binding energies of oxygenated species on the surface.

The potentials of redox transitions in metal oxides can scale with the binding energies of oxygenated species and correlate with ORR activity. This hypothesis is supported by a recent study of ORR activity of metal-nitrogen-based catalysts involving moieties containing a metal center coordinated by four pyrrolic nitrogen atoms (MN4), as shown in Figures 6A and 6B. Increasing the experimental redox potential of M²⁺/M³⁺ couple for these MN4 catalysts is shown to scale with decreasing the computed binding energy of oxygen, which leads to increasing ORR activity, as shown in Figure 6C.¹¹⁸ The highest ORR activities can be obtained for M²⁺/M³⁺ redox potentials around +1.2 V_{RHE} (pH 13) for metal phthalocyanines (MPc) when M = Fe.¹¹⁹

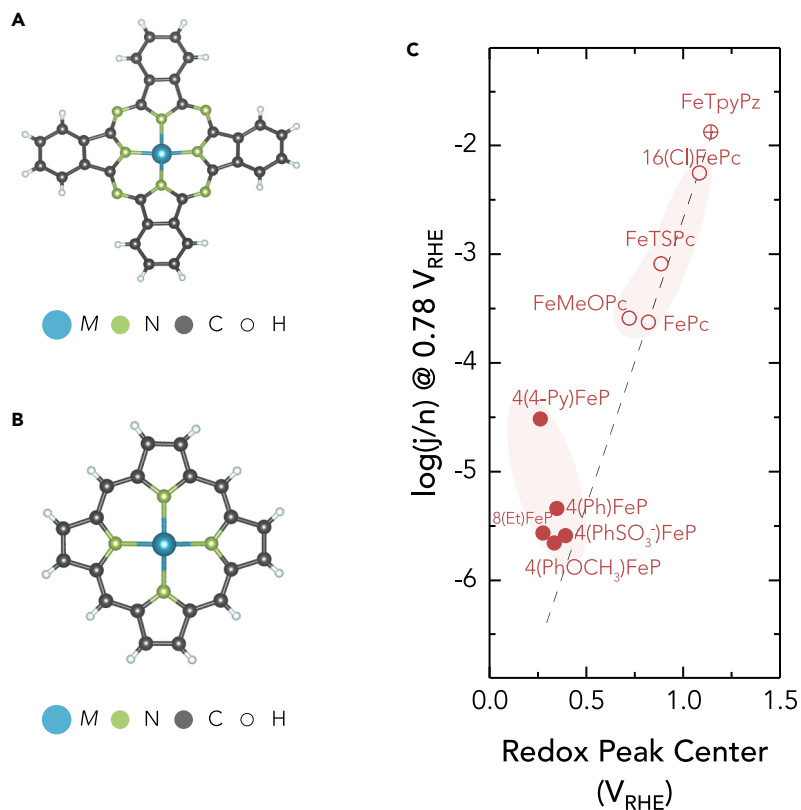


Figure 6. Scaling between ORR Activity and Redox Peak Position for MN4 Compounds

(A–C) Representations of the molecular structure of (A) Mpc (metal phthalocyanine), (B) MP (metal porphyrin), and (C) Catalytic activities in ORR (j/n , where j is current density, n is number of electrons transferred; $n = 4$) in alkaline media (pH 13) recorded at 0.78 V versus RHE for different Fe-based catalysts.¹¹⁸

ORR activity of inverse spinels $[X_xFe^{2+}_{1-x}]_{\text{oct}}[Fe^{3+}]_{\text{tetra}}[Fe^{3+}]_{\text{oct}}O_4$ ($X = \text{Mn}$)¹²⁰ in 0.1 M KOH was found to increase with the greater formal potential of Fe^{2+}/Fe^{3+} redox on the octahedral site at $\sim 0.5 V_{RHE}$, as shown in Figure 7B. The anodic shift of Fe^{2+}/Fe^{3+} redox couple in a row of Mn-Fe spinels can be explained, in our opinion, analogously to the case of Li-intercalation potential changes in $\text{LiFe}_{1-x}\text{Mn}_x\text{PO}_4$ solid solutions (see discussion in Fe-Based Oxides), where structural effects were shown to dominate over inductive effect.⁵⁰ In the case of substituted Fe spinels, structural changes caused by Fe-to-Mn substitution might also affect the covalency of the Fe-O bond, thus shifting the potential in the anodic direction. Extending such a trend shown in Figure 7B to more substituents in $[X_xFe^{2+}_{1-x}]_{\text{oct}}[Fe^{3+}]_{\text{tetra}}[Fe^{3+}]_{\text{oct}}O_4$ ¹²⁰ was not possible due to lack of redox features reported. We correlated increasing ORR activity of $[X_xFe^{2+}_{1-x}]_{\text{oct}}[Fe^{3+}]_{\text{tetra}}[Fe^{3+}]_{\text{oct}}O_4$ ¹²⁰ (Fe_3O_4 , $\text{Cu}_{0.7}\text{Fe}_{2.3}\text{O}_4$, $\text{Co}_{0.8}\text{Fe}_{2.2}\text{O}_4$, and $\text{Mn}_{0.6}\text{Fe}_{2.4}\text{O}_4$) and $X\text{Co}_2\text{O}_4$ ¹²¹ (Co_3O_4 , ZnCo_2O_4 , and NiCo_2O_4) spinels with decreasing electronegativity of X^{2+} substituent or increasing pK_a of $[X(\text{H}_2\text{O})_m]^{n+}$ (Figure S12). Following the concept in Figures 1, 2, and 3, the increasing ORR activity (Figure S12) should scale with decreasing redox potential of Fe^{2+}/Fe^{3+} , which contrasts with that in Figure 7B. These data points, however, might correspond to the descending portion of the ORR volcano, where decreasing redox potential would lead to stronger binding and increased ORR activity, explaining the apparent discrepancy; however, this requires further studies.

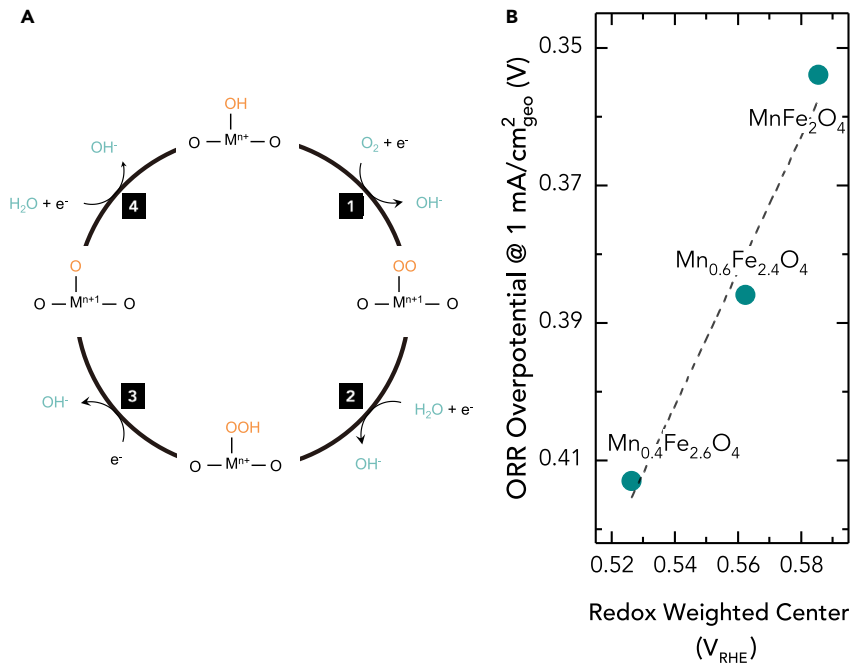


Figure 7. Scaling between ORR Activity and Redox Peak Position for Fe-Based Spinel Oxides

(A) Conventional ORR mechanism reported previously for metal oxides in basic solution.^{27,106} (B) ORR activity of $X_x\text{Fe}^{2+}_{1-x}\text{Fe}^{3+}_x\text{O}_4$ inverse spinels as a function of $\text{Fe}^{2+}/\text{Fe}^{3+}$ redox peak position. ORR measurements were performed in O_2 -saturated 0.1 M KOH with a spin rate of 1,600 rpm and with scan rates of 10 mV/s.¹²⁰ The oxide loadings were $\sim 80 \mu\text{g}/\text{cm}^2_{\text{geo}}$.¹²⁰ The weighted centers were calculated as schematically depicted in Figures S1–S3.

OER Activity

Here we relate the OER activity of metal oxides to the potential of redox processes preceding OER, which also corresponds to the redox of surface metal ion sites, $[\text{M}^{n+}\text{-OH}_{\text{ad}}]/[\text{M}^{n+1}\text{-O}_{\text{ad}}]$ in the conventional mechanism, as shown in Figure 8A. The OER activity of substituted nickel hydroxides (Figure 3E) was shown to increase with the greater potential of the redox event (at $\sim 1.4 \text{ V}_{\text{RHE}}$) upon substitution of metals with greater electronegativity, as shown in Figure 8B. This trend is further supported by the results previously reported for Ni-Fe⁸³ (hydr-)oxides with different concentration of Fe substitution, where increasing OER activity is accompanied by increasing redox potentials, as shown in Figure 8C. Further support came from correlations of increasing OER activity with increasing electronegativity of metal substituent in $\text{Ni}(\text{OH})_2$ and decreasing pK_a from Mn^{2+} to Fe^{3+} (Figure S11). These observations can be rationalized by the following arguments. Increasing the redox potential of the process centered at $\sim 1.4 \text{ V}$, which has been assigned to $\text{Ni}^{3+}\text{OOH} + x\text{OH}^- \rightarrow \text{Ni}^{3+x}\text{O}_{1+x}(\text{OH})_{1-x} + x\text{H}_2\text{O} + xe^-$, would increase $\Delta G_{\text{Oad}} - \Delta G_{\text{OHad}}$ on surface Ni sites, and increase the OER activity by reducing the barrier associated with the rate-limiting step ($[\text{M}^{n+}\text{-O}] + \text{OH}^- \rightarrow [\text{M}^{n+1}\text{-OOH}] + e^-$). X-ray spectroscopy measurements confirm the involvement of Ni^{4+} in this redox process. The work of Friebel et al.¹²² shows OER-active species involving nominal Ni^{4+} and Fe^{3+} in $(\text{Ni},\text{Fe})\text{OOH}$, and Li et al.¹²³ report a maximum mixed-valence resting state of 3.6+ attained for Ni ions with 4 mol% Fe substitution.

In addition, recent XAS measurements¹²⁴ show that Ni oxidation state in Ni-Fe (hydr-)oxides is lower than that in Ni-based (hydr-)oxide at OER-relevant potentials

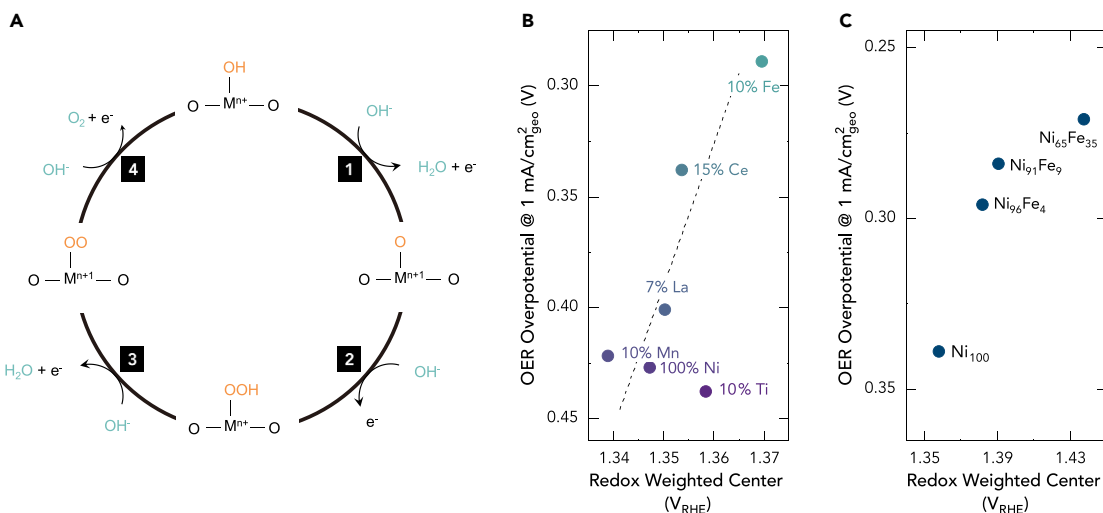


Figure 8. Scaling between OER Activity and Redox Peak Position for Ni-Based Hydroxides

(A) Conventional OER mechanism proposed for metal oxides¹⁰⁸ with four steps: 1, surface hydroxide deprotonation; 2, surface peroxide formation; 3, surface peroxide deprotonation; 4, surface hydroxide regeneration.

(B) The relationship between the OER activity and the weighted center position of the Ni redox peaks for X-doped nickel hydroxides. The OER activity was extracted using previous work,¹⁹ where the measurements were performed for spin-cast films ($4\text{--}5 \mu\text{g}_{\text{oxide}}/\text{cm}^2_{\text{geo}}$) in O_2 -saturated 1 M KOH, with the scan rate of 20 mV/s.

(C) The relationship between the OER activity and the weighted center position of the Ni redox peaks for Fe-Ni hydroxides. The OER activity was extracted using previous work,⁸³ where the measurements were performed for drop-cast films ($5 \mu\text{g}_{\text{oxide}}/\text{cm}^2_{\text{geo}}$) in N_2 -saturated 0.1 M KOH, with the scan rate of 10 mV/s. The weighted centers were calculated as schematically depicted in Figures S1–S3.

(1.63 V_{RHE}). OER catalyzed by Ni-Fe (hydr-)oxides can involve more oxygen associated with oxide lattice,^{83,124} thus deviating from the conventional mechanism, where reduction of nickel sites upon oxygen release may occur, competing with nickel oxidation during OER. Having filled metal antibonding states, such as those of nominal $\text{Ni}^{3+}/4^+$ and $\text{Co}^{3+}/4^+$, falling below the top of the O p band would promote the mechanism of oxygen evolution involving oxide lattice, which is supported by recent experimental studies for $\text{SrCoO}_{3-\delta}$.¹⁵ Formation of tetravalent nickel peroxide species (e.g., nominal $\text{Ni}^{4+}\text{-OO}$)¹²² further supports this mechanism. Moreover, Ni-Fe (hydr-)oxides exhibit pH-dependent activity on the RHE scale,¹²⁴ which is typically accompanied with the involvement of the lattice oxygen in the OER^{15,93,125,126} ($[\text{O}_{\text{lattice}}] + \text{OH}^- \rightarrow [\text{O}_{\text{lattice}} - \text{OH}_{\text{ad}}] + \text{e}^-$). Altogether, this allows us to assume that high activity of Ni-Fe (hydr-)oxide systems originates from its functioning through the OER mechanism involving lattice oxygen participation.

High activity of Ni-Fe oxyhydroxide is also attributed to a change of the active site from nickel to iron^{22,122,127–129} rather than the effect of substituent on the electronic state of the parent metal Ni. Higher bulk electronic conductivity of NiOOH matrix compared with FeOOH could result in a dramatic increase of the number of accessible active sites¹³⁰ rendering high OER activity. Functioning of iron as an active site is supported by computational¹²² and mechanistic^{127–129} studies showing faster OER kinetics on Fe centers.

A recent study has demonstrated that OER activity of Ni-Fe layered double hydroxides increases with decreasing standard redox potential of anions intercalated in the interlayers.¹³¹ This trend was attributed by authors to the enhanced electron-donating ability of the anions with low redox potentials (e.g., H_2PO_2^-) which increase the electron density on transition metal ions, thus stabilizing the

higher oxidation state of metal. This trend can apparently be explained by the inductive effect whereby anions characterizing with weaker electron-donating ability (e.g., F^-) would lead to an increased ionicity of the M-O bond, which is confirmed by DFT calculations indicating the increase of the Bader charges on both Ni and Fe sites upon intercalation with fewer electron-donating anions.¹³¹ Like the case of substituted Co- and Fe-based spinels discussed above (see Figure S12), these electronic effects lead to increased catalytic activity assuming that linear dependence between OER activity and redox potential of anions¹³¹ might correspond to the ascending portion of the volcano trend. However, different accessibility of the active sites due to varied interlayer distance, which scales with anion size, can also influence the OER activity trend.

Similar to the case of $LiFe_xX_{1-x}PO_4$, discussed in Fe-Based Oxides, the influence of the inductive effect on the OER activity can be outweighed by other factors. For example, for $(Ln_{0.5}Ba_{0.5})CoO_{3-\delta}$ double perovskites,²⁶ it was shown that the change of the formal oxidation state of cobalt upon different Ln^{3+} substitution is a primary factor defining the relative position of O p-band center and Fermi level in these materials, rather than changes of electronegativity/Lewis acidity of Ln^{3+} .

Although the OER activity of metal oxides can be correlated with the potential of redox preceding OER (Figure 8), there is no good agreement between estimated values of $\Delta G_{Oad} - \Delta G_{OHad}$ from the redox potential (eU_{RHE}) and $\Delta G_{Oad} - \Delta G_{OHad}$ computed with generalized gradient approximation with Hubbard U applied (GGA + U) (Figure S13). For example, the experimental potential of the redox event for IrO_2 (110) prior to OER occurs at $\sim 1.5 V_{RHE}$,¹¹⁴ while that for RuO_2 (110)^{132,133} takes place at a lower voltage, $\sim 1.35 V_{RHE}$, which is typically assigned to $[M^{n+}-OH]/[M^{n+1}-O]$ or $[M^{n+}-OH] = [M^{n+1}-O] + H^+ + e^-$.^{134,135} However, the computed value of $\Delta G_O^* - \Delta G_{OH}^*$ on IrO_2 (110) is lower than that of RuO_2 (110).^{106,107} The discrepancy can be attributed to the fact that the redox process preceding OER on metal oxide surfaces might not correspond to the transition from OH_{ad} to O_{ad} , where the mechanistic details should be studied further in more detail. For example, these redox transitions might not result in a complete change of all OH_{ad} groups to O_{ad} , and partial coverage may be stabilized at different potentials due to adsorbate interactions. Furthermore, interactions between surface-adsorbed species can lead to different stabilized adsorbed intermediates at these potentials.¹³⁶ Further investigations on the nature of the redox active site and surface termination of oxides *in situ* during OER is critical in providing mechanistic details between redox peak positions and binding energetics of key OER intermediates, which could potentially provide exciting opportunities to affect OER activity by tuning the potentials of relevant redox events.

In general, the redox potential position can be used as an effective descriptor for the ORR/OER activity of metal-substituted (hydr-)oxides catalysts, which reflects the influence of the inductive effect of foreign metals on the electronic structure and, thus, to the surface oxygen adsorption strength. Shifting the redox potential positively can often lead to higher catalytic activity that can be used to guide the metal substitution to improve the (hydr-)oxide catalyst performance.

Conclusions

In this review, we have examined the influence of the inductive effect associated with metal substitutions on the redox process of transition metals in metal complexes, lithium transition metal oxides, and Ni, Co, Fe-based hydr-(oxides) used

for ORR/OER electrocatalysis. We introduce a universal origin for the inductive effect associated with metal substitutions in these systems. Substitution by metal ions (X^{n+}) with greater electronegativity and lower pK_a of $[X(H_2O)_m]^{n+}$ is shown to positively shift the formal redox potential of parent metal in transition metal complexes and (hydr-)oxides. Such observations can be rationalized by inductive effect: substitution with elements of higher electronegativity compared with parent metal would lead to lowering of the electron energy associated with the antibonding states of metal-ligand (e.g., oxygen), which is accompanied with the shift of the electron density from parent metal to ligand. Moreover, tuning the redox potential of metal complexes and metal (hydr-)oxides can lead to greater ORR/OER activity, which can be attributed to optimized binding of the reaction intermediates on the surface in rate-limiting steps. Such findings demonstrate exciting opportunities to enhance the activity of catalysts by controlling redox processes adjacent to reactions of interest.

Methodology and Measurements

The CV curves of nickel perovskite oxides in Figure 3D were measured using a rotating-disk electrode setup in O_2 -saturated 0.1 M KOH electrolyte with the scan rate of 10 mV/s. The voltage loss from ohmic resistance in these measurements have been corrected using $E - iR$, where E is the measured voltage, i is the measured current, and R is the ohmic resistance measured by impedance. The weighted centers of oxidation and reduction processes in Figures 3E and 3F were determined by applying the function $V_{\text{weighted}} = \int V dQ / \int dQ$ on the oxidation and reduction peaks, respectively, after the linear double-layer-capacitance background correction, where Q is the corresponding charge transfer at the voltage V in the redox process. The average value of the oxidation and reduction weighted centers was then used as the redox-weighted center on the plots (see Figures S1–S3). The activity data and the position of the corresponding redox peaks for metal-substituted compounds $[LXMn_3O_4(OAc)_3(L')]^{n+}$ ³⁶ $[LXFe_3O(OH)_-(OTf)_y(L')]^{m+}$ ³⁷ $Ni(OH)_2$ ¹⁹ $Co_{1-x}Fe_xO_yH_z$ ³⁸ $Ni_{1-x}Fe_xO_yH_z$ ⁸³ $M_xFe^{2+}_{1-x}Fe^{3+}_{2-x}O_4$ ¹²⁰ and MCo_2O_4 ¹²¹ were extracted from the literature (detailed procedures are described in Figures S6–S8 and S10). The first discharge curve of Li-ion battery materials from previous work^{39–41,104} was smoothed with moving average filter and the first derivative of the capacity with regard to voltage (dQ/dV) was taken, where the peak of dQ/dV was extracted as the Li-intercalation potential; this process is schematically shown in Figure S4, while all the raw data used to generate Figure 5 are shown in Figure S5. For metal-substituted $LiCoO_2$, since the charge profile in the first cycle was also available, the average value of Li-intercalation/de-intercalation voltage was taken as the intercalation voltage. The values of crystal radii of ions (designated as ionic radii throughout the paper) in Figure 3 were taken from Shannon.¹³⁷

SUPPLEMENTAL INFORMATION

Supplemental Information includes 14 figures and can be found with this article online at <https://doi.org/10.1016/j.joule.2017.11.014>.

ACKNOWLEDGMENTS

This work was supported by the Toyota Research Institute through the Accelerated Materials Design and Discovery program. The authors would like to acknowledge Kevin May and Jin Suntivich for collected cyclic voltammetry measurements of Ni-based perovskites, and Alexis Grimaud and Marcel Risch for initial analysis of redox potentials of metal oxides and fruitful discussion.

REFERENCES

1. Schipper, F., Erickson, E.M., Erk, C., Shin, J.-Y., Chesneau, F.F., and Aurbach, D. (2017). Recent advances and remaining challenges for lithium ion battery cathodes I. Nickel-Rich, $\text{LiNi}_x\text{Co}_y\text{Mn}_2\text{O}_2$. *J. Electrochem. Soc.* 164, A6220–A6228.
2. Slater, M.D., Kim, D., Lee, E., and Johnson, C.S. (2013). Sodium-ion batteries. *Adv. Funct. Mater.* 23, 947–958.
3. Kim, S.-W., Seo, D.-H., Ma, X., Ceder, G., and Kang, K. (2012). Electrode materials for rechargeable sodium-ion batteries: potential alternatives to current lithium-ion batteries. *Adv. Energ. Mater.* 2, 710–721.
4. Wang, G., Zhang, L., and Zhang, J. (2012). A review of electrode materials for electrochemical supercapacitors. *Chem. Soc. Rev.* 41, 797–828.
5. Chen, S.-M., Ramachandran, R., Mani, V., and Sarawathi, R. (2014). Recent advancements in electrode materials for the high-performance electrochemical supercapacitors: a review. *Int. J. Electrochem. Sci.* 9, 4072–4085.
6. Osgood, H., Devaguptapu, S.V., Xu, H., Cho, J., and Wu, G. (2016). Transition metal (Fe, Co, Ni, and Mn) oxides for oxygen reduction and evolution bifunctional catalysts in alkaline media. *Nano Today* 11, 601–625.
7. Stoerzinger, K.A., Risch, M., Han, B., and Shao-Horn, Y. (2015). Recent insights into manganese oxides in catalyzing oxygen reduction kinetics. *ACS Catal.* 5, 6021–6031.
8. Hunter, B.M., Gray, H.B., and Müller, A.M. (2016). Earth-abundant heterogeneous water oxidation catalysts. *Chem. Rev.* 116, 14120–14136.
9. Han, L., Dong, S., and Wang, E. (2016). Transition-metal (Co, Ni, and Fe)-based electrocatalysts for the water oxidation reaction. *Adv. Mater.* 28, 9266–9291.
10. Gasteiger, H.A., Kocha, S.S., Sompalli, B., and Wagner, F.T. (2005). Activity benchmarks and requirements for Pt, Pt-alloy, and non-Pt oxygen reduction catalysts for PEMFCs. *Appl. Catal. B Environ.* 56, 9–35.
11. McCrory, C.C.L., Jung, S., Peters, J.C., and Jarillo, T.F. (2013). Benchmarking heterogeneous electrocatalysts for the oxygen evolution reaction. *J. Am. Chem. Soc.* 135, 16977–16987.
12. Armand, M., and Tarascon, J.M. (2008). Building better batteries. *Nature* 451, 652–657.
13. Meyer, T.J. (2008). Catalysis: the art of splitting water. *Nature* 451, 778–779.
14. Gray, H.B. (2009). Powering the planet with solar fuel. *Nat. Chem.* 1, 7.
15. Grimaud, A., Diaz-Morales, O., Han, B., Hong, W.T., Lee, Y.-L., Giordano, L., Stoerzinger, K.A., Koper, M.T., and Shao-Horn, Y. (2017). Activating lattice oxygen redox reactions in metal oxides to catalyze oxygen evolution. *Nat. Chem.* 9, 457–465.
16. Zhong, Q., Bonakdarpour, A., Zhang, M., Gao, Y., and Dahn, J. (1997). Synthesis and electrochemistry of $\text{LiNi}_x\text{Mn}_{2-x}\text{O}_4$. *J. Electrochem. Soc.* 144, 205–213.
17. Ohzuku, T., and Makimura, Y. (2001). Layered lithium insertion material of $\text{LiNi}_{1/2}\text{Mn}_{1/2}\text{O}_2$: a possible alternative to LiCoO_2 for advanced lithium-ion batteries. *Chem. Lett.* 30, 744–745.
18. Sathiya, M., Ramesha, K., Rousse, G., Foix, D., Gonbeau, D., Prakash, A., Doublet, M., Hemalatha, K., and Tarascon, J.-M. (2013). High performance $\text{Li}_{2-x}\text{Ru}_{1-y}\text{Mn}_y\text{O}_3$ ($0.2 \leq y \leq 0.8$) cathode materials for rechargeable lithium-ion batteries: their understanding. *Chem. Mater.* 25, 1121–1131.
19. Enman, L.J., Burke, M.S., Batcheller, A.S., and Boettcher, S.W. (2016). Effects of intentionally incorporated metal cations on the oxygen evolution electrocatalytic activity of nickel (oxy) hydroxide in alkaline media. *ACS Catal.* 6, 2416–2423.
20. Trotochaud, L., Young, S.L., Ranney, J.K., and Boettcher, S.W. (2014). Nickel-iron oxyhydroxide oxygen-evolution electrocatalysts: the role of intentional and incidental iron incorporation. *J. Am. Chem. Soc.* 136, 6744–6753.
21. Trotochaud, L., Ranney, J.K., Williams, K.N., and Boettcher, S.W. (2012). Solution-cast metal oxide thin film electrocatalysts for oxygen evolution. *J. Am. Chem. Soc.* 134, 17253–17261.
22. Diaz-Morales, O., Ledezma-Yanez, I., Koper, M.T., and Calle-Vallejo, F. (2015). Guidelines for the rational design of Ni-based double hydroxide electrocatalysts for the oxygen evolution reaction. *ACS Catal.* 5, 5380–5387.
23. Garcia-Mota, M., Vojvodic, A., Metiu, H., Man, I.C., Su, H.Y., Rossmeisl, J., and Nørskov, J.K. (2011). Tailoring the activity for oxygen evolution electrocatalysis on Rutile $\text{TiO}_2(110)$ by transition-metal substitution. *ChemCatChem* 3, 1607–1611.
24. Suntivich, J., May, K.J., Gasteiger, H.A., Goodenough, J.B., and Shao-Horn, Y. (2011). A perovskite oxide optimized for oxygen evolution catalysis from molecular orbital principles. *Science* 334, 1383–1385.
25. Mefford, J.T., Rong, X., Abakumov, A.M., Hardin, W.G., Dai, S., Kolpak, A.M., Johnston, K.P., and Stevenson, K.J. (2016). Water electrolysis on $\text{La}_{1-x}\text{Sr}_x\text{CoO}_{3-\delta}$ perovskite electrocatalysts. *Nat. Commun.* 7, 11053.
26. Grimaud, A., May, K.J., Carlton, C.E., Lee, Y.-L., Risch, M., Hong, W.T., Zhou, J., and Shao-Horn, Y. (2013). Double perovskites as a family of highly active catalysts for oxygen evolution in alkaline solution. *Nat. Comm.* 4, 2439.
27. Suntivich, J., Gasteiger, H.A., Yabuuchi, N., Nakanishi, H., Goodenough, J.B., and Shao-Horn, Y. (2011). Design principles for oxygen-reduction activity on perovskite oxide catalysts for fuel cells and metal-air batteries. *Nat. Chem.* 3, 546–550.
28. Dokko, K., Mohamedi, M., Anzue, N., Itoh, T., and Uchida, I. (2002). In situ Raman spectroscopic studies of $\text{LiNi}_x\text{Mn}_{2-x}\text{O}_4$ thin film cathode materials for lithium ion secondary batteries. *J. Mater. Chem.* 12, 3688–3693.
29. Desilvestro, J., Corrigan, D.A., and Weaver, M.J. (1988). Characterization of redox states of nickel hydroxide film electrodes by in situ surface Raman spectroscopy. *J. Electrochem. Soc.* 135, 885–892.
30. Liu, H., Bugnet, M., Tessaro, M.Z., Harris, K.J., Dunham, M.J., Jiang, M., Goward, G.R., and Botton, G.A. (2016). Spatially resolved surface valence gradient and structural transformation of lithium transition metal oxides in lithium-ion batteries. *Phys. Chem. Chem. Phys.* 18, 29064–29075.
31. Starr, D., Liu, Z., Hävecker, M., Knop-Gericke, A., and Bluhm, H. (2013). Investigation of solid/vapor interfaces using ambient pressure X-ray photoelectron spectroscopy. *Chem. Soc. Rev.* 42, 5833–5857.
32. Stoerzinger, K.A., Hong, W.T., Crumlin, E.J., Bluhm, H., and Shao-Horn, Y. (2015). Insights into electrochemical reactions from ambient pressure photoelectron spectroscopy. *Acc. Chem. Res.* 48, 2976–2983.
33. Konezny, S.J., Doherty, M.D., Luca, O.R., Crabtree, R.H., Soloveichik, G.L., and Batista, V.S. (2012). Reduction of systematic uncertainty in DFT redox potentials of transition-metal complexes. *J. Phys. Chem. C* 116, 6349–6356.
34. Mavros, M.G., Tsuchimochi, T., Kowalczyk, T., McIsaac, A., Wang, L.P., and Voorhis, T.V. (2014). What can density functional theory tell us about artificial catalytic water splitting? *Inorg. Chem.* 53, 6386–6397.
35. Ong, S.P., Chevrier, V.L., Hautier, G., Jain, A., Moore, C., Kim, S., Ma, X., and Ceder, G. (2011). Voltage, stability and diffusion barrier differences between sodium-ion and lithium-ion intercalation materials. *Energ. Environ. Sci.* 4, 3680–3688.
36. Tsui, E.Y., and Agapie, T. (2013). Reduction potentials of heterometallic manganese-oxido cubane complexes modulated by redox-inactive metals. *Proc. Natl. Acad. Sci. USA* 110, 10084–10088.
37. Herbert, D.E., Lionetti, D., Rittle, J., and Agapie, T. (2013). Heterometallic trirrion-oxo/hydroxo clusters: effect of redox-inactive metals. *J. Am. Chem. Soc.* 135, 19075–19078.
38. Burke, M.S., Kast, M.G., Trotochaud, L., Smith, A.M., and Boettcher, S.W. (2015). Cobalt-iron (oxy) hydroxide oxygen evolution electrocatalysts: the role of structure and composition on activity, stability, and mechanism. *J. Am. Chem. Soc.* 137, 3638–3648.
39. Kim, H.-S., Ko, T.-K., Na, B.-K., Cho, W.I., and Chao, B.W. (2004). Electrochemical properties of $\text{Li}_M\text{Co}_{1-x}\text{O}_2$ [$M = \text{Mg}, \text{Zr}$] prepared by sol-gel process. *J. Power Sourc.* 138, 232–239.
40. Eom, J., and Cho, J. (2008). $\text{M}_3(\text{PO}_4)_2$ -nanoparticle-coated LiCoO_2 vs $\text{LiCo}_{0.96}\text{M}_{0.04}\text{O}_2$ [$M = \text{Mg}$ and Zn] on electrochemical and storage characteristics. *J. Electrochem. Soc.* 155, A201–A205.

41. Zou, M., Yoshio, M., Gopukumar, S., and Yamaki, J.I. (2004). Synthesis and electrochemical performance of high voltage cycling $\text{LiM}_{0.05}\text{Co}_{0.95}\text{O}_2$ as cathode material for lithium rechargeable cells. *Electrochim. Solid State Lett.* 7, A176–A179.
42. Stephens, I.E., Bondarenko, A.S., Grønbjerg, U., Rossmeisl, J., and Chorkendorff, I. (2012). Understanding the electrocatalysis of oxygen reduction on platinum and its alloys. *Energ. Environ. Sci.* 5, 6744–6762.
43. Muller, P. (1994). Glossary of terms used in physical organic chemistry (IUPAC Recommendations 1994). *Pure Appl. Chem.* 66, 1077–1184.
44. Wade, L.G., Jr. (2013). *Organic Chemistry*, Eighth Edition (Pearson).
45. Stock, L.M. (1972). The origin of the inductive effect. *J. Chem. Educ.* 49, 400–404.
46. Manthiram, A., and Goodenough, J. (1987). Lithium insertion into $\text{Fe}_2(\text{MO}_4)_3$ frameworks: comparison of M= W with M= Mo. *J. Solid State Chem.* 71, 349–360.
47. Manthiram, A., and Goodenough, J. (1989). Lithium insertion into $\text{Fe}_2(\text{SO}_4)_3$ frameworks. *J. Power Sourc.* 26, 403–408.
48. Padhi, A., Nanjundaswamy, K., Masquelier, C., Okada, S., and Goodenough, J. (1997). Effect of structure on the $\text{Fe}^{3+}/\text{Fe}^{2+}$ redox couple in iron phosphates. *J. Electrochem. Soc.* 144, 1609–1613.
49. Goodenough, J.B., and Kim, Y. (2009). Challenges for rechargeable Li batteries. *Chem. Mater.* 22, 587–603.
50. Muraliganth, T., and Manthiram, A. (2010). Understanding the shifts in the redox potentials of olivine $\text{LiM}_{1-y}\text{MyPO}_4$ (M= Fe, Mn, Co, and Mg) solid solution cathodes. *J. Phys. Chem. C* 114, 15530–15540.
51. Omenya, F., Wen, B., Fang, J., Zhang, R., Wang, Q., Chernova, N.A., Schneider-Haefner, J., Cosandey, F., and Whittingham, M.S. (2015). Mg substitution clarifies the reaction mechanism of olivine LiFePO_4 . *Adv. Energ. Mater.* 5. <https://doi.org/10.1002/aem.201401204>.
52. Tsui, E.Y., Tran, R., Yano, J., and Agapie, T. (2013). Redox-inactive metals modulate the reduction potential in heterometallic-manganese-oxido clusters. *Nat. Chem.* 5, 293–299.
53. Lin, P.H., Takase, M.K., and Agapie, T. (2014). Investigations of the effect of the non-manganese metal in heterometallic-oxido cluster models of the oxygen evolving complex of photosystem II: lanthanides as substitutes for calcium. *Inorg. Chem.* 54, 59–64.
54. Vrettos, J.S., Stone, D.A., and Brudvig, G.W. (2001). Quantifying the ion selectivity of the Ca^{2+} site in photosystem II: evidence for direct involvement of Ca^{2+} in O_2 formation. *Biochemistry* 40, 7937–7945.
55. Lee, C.I., Lakshmi, K., and Brudvig, G.W. (2007). Probing the functional role of Ca^{2+} in the oxygen-evolving complex of photosystem II by metal ion inhibition. *Biochemistry* 46, 3211–3223.
56. Krewald, V., Neese, F., and Pantazis, D.A. (2016). Redox potential tuning by redox-inactive cations in nature's water oxidizing catalyst and synthetic analogues. *Phys. Chem. Chem. Phys.* 18, 10739–10750.
57. Pavlishchuk, V.V., and Addison, A.W. (2000). Conversion constants for redox potentials measured versus different reference electrodes in acetonitrile solutions at 25 C. *Inorg. Chim. Acta* 298, 97–102.
58. Perrin, D.D. (2016). *Ionisation Constants of Inorganic Acids and Bases in Aqueous Solution*, Vol. 29 (Elsevier).
59. Wang, J., Cui, W., Liu, Q., Xing, Z., Asiri, A.M., and Sun, X. (2016). Recent progress in cobalt-based heterogeneous catalysts for electrochemical water splitting. *Adv. Mater.* 28, 215–230.
60. Gao, M., Sheng, W., Zhuang, Z., Fang, Q., Gu, S., Jiang, J., and Yan, Y. (2014). Efficient water oxidation using nanostructured α -nickel-hydroxide as an electrocatalyst. *J. Am. Chem. Soc.* 136, 7077–7084.
61. Whittingham, M.S. (2004). Lithium batteries and cathode materials. *Chem. Rev.* 104, 4271–4301.
62. Rouxel, J. (1996). Anion-cation redox competition and the formation of new compounds in highly covalent systems. *Chem. A Eur. J.* 2, 1053–1059.
63. Wu, E.J., Tepesch, P.D., and Ceder, G. (1998). Size and charge effects on the structural stability of LiMO_2 (M= transition metal) compounds. *Philosophical Mag. B* 77, 1039–1047.
64. Grimaud, A., Hong, W., Shao-Horn, Y., and Tarascon, J.M. (2016). Anionic redox processes for electrochemical devices. *Nat. Mater.* 15, 121–126.
65. Trasatti, S. (1986). The absolute electrode potential: an explanatory note (Recommendations 1986). *Pure Appl. Chem.* 58, 955–966.
66. Mizushima, K., Jones, P., Wiseman, P., and Goodenough, J.B. (1980). Li_xCoO_2 ($0 < x < 1$): a new cathode material for batteries of high energy density. *Mater. Res. Bull.* 15, 783–789.
67. Padhi, A.K., Nanjundaswamy, K., and Goodenough, J.B. (1997). Phospho-olivines as positive-electrode materials for rechargeable lithium batteries. *J. Electrochem. Soc.* 144, 1188–1194.
68. Hong, W.T., Stoerzinger, K.A., Moritz, B., Devereaux, T.P., Yang, W., and Shao-Horn, Y. (2015). Probing LaMO_3 metal and oxygen partial density of states using X-ray emission, absorption, and photoelectron spectroscopy. *J. Phys. Chem. C* 119, 2063–2072.
69. Kosmulski, M. (2016). Isoelectric points and points of zero charge of metal (hydr) oxides: 50 years after Parks' review. *Adv. Colloid Interf. Sci.* 238, 1–61.
70. Corrigan, D.A., and Bendert, R.M. (1989). Effect of coprecipitated metal ions on the electrochemistry of nickel hydroxide thin films: cyclic voltammetry in 1M KOH. *J. Electrochim. Soc.* 136, 723–728.
71. Merrill, M., Worsley, M., Wittstock, A., Biener, J., and Stadermann, M. (2014). Determination of the "NiOOH" charge and discharge mechanisms at ideal activity. *J. Electroanal. Chem.* 717, 177–188.
72. Trześniewski, B.J., Diaz-Morales, O., Vermaas, D.A., Longo, A., Bras, W., Koper, M.T., and Smith, W.A. (2015). In situ observation of active oxygen species in Fe-containing Ni-based oxygen evolution catalysts: the effect of pH on electrochemical activity. *J. Am. Chem. Soc.* 137, 15112–15121.
73. Diaz-Morales, O., Ferrus-Suspiedra, D., and Koper, M.T. (2016). The importance of nickel oxyhydroxide deprotonation on its activity towards electrochemical water oxidation. *Chem. Sci.* 7, 2639–2645.
74. Bode, H., Dehmelt, K., and Witte, J. (1966). Zur Kenntnis der nickelhydroxidelektrode—I. Über das nickel (II)-hydroxidhydrat. *Electrochim. Acta* 11, 1079–1087.
75. Oliva, P., Leonardi, J., Laurent, J., Delmas, C., Braconnier, J., Figlarz, M., Fievet, F., and De Guibert, A. (1982). Review of the structure and the electrochemistry of nickel hydroxides and oxy-hydroxides. *J. Power Sourc.* 8, 229–255.
76. Rebouillat, S., Lyons, M.E., Brandon, M.P., and Doyle, R.L. (2011). Paving the way to the integration of smart nanostructures: part II: nanostructured microdispersed hydrated metal oxides for electrochemical energy conversion and storage applications. *Int. J. Electrochim. Sci.* 6, 5830–5917.
77. Doyle, R.L., Godwin, I.J., Brandon, M.P., and Lyons, M.E. (2013). Redox and electrochemical water splitting catalytic properties of hydrated metal oxide modified electrodes. *Phys. Chem. Chem. Phys.* 15, 13737–13783.
78. Beverskog, B., and Puigdomenech, I. (1997). Revised Pourbaix diagrams for nickel at 25–300 C. *Corros. Sci.* 39, 969–980.
79. Louie, M.W., and Bell, A.T. (2013). An investigation of thin-film Ni-Fe oxide catalysts for the electrochemical evolution of oxygen. *J. Am. Chem. Soc.* 135, 12329–12337.
80. Juodkazis, K., Juodkazyté, J., Vilkauskaitė, R., and Jasulaitienė, V. (2008). Nickel surface anodic oxidation and electrocatalysis of oxygen evolution. *J. Solid State Electrochem.* 12, 1469–1479.
81. Zeng, Z., Chan, M.K., Zhao, Z.-J., Kubal, J., Fan, D., and Greeley, J. (2015). Towards first principles-based prediction of highly accurate electrochemical Pourbaix diagrams. *J. Phys. Chem. C* 119, 18177–18187.
82. Wang, D., Zhou, J., Hu, Y., Yang, J., Han, N., Li, Y., and Sham, T.-K. (2015). In situ X-ray absorption near-edge structure study of advanced NiFe(OH)_x electrocatalyst on carbon paper for water oxidation. *J. Phys. Chem. C* 119, 19573–19583.
83. Görlin, M., Chernev, P., de Araujo, J.F., Reier, T., Dresp, S., Paul, B., Krähnert, R., Dau, H., and Strasser, P. (2016). Oxygen evolution reaction dynamics, Faradaic charge efficiency, and the active metal redox states of Ni-Fe oxide water splitting electrocatalysts. *J. Am. Chem. Soc.* 138, 5603–5614.

84. Bediako, D.K., Lassalle-Kaiser, B., Surendranath, Y., Yano, J., Yachandra, V.K., and Nocera, D.G. (2012). Structure-activity correlations in a nickel-borate oxygen evolution catalyst. *J. Am. Chem. Soc.* 134, 6801–6809.
85. O'Grady, W.E., Pandya, K.I., Swider, K.E., and Corrigan, D.A. (1996). In situ X-ray absorption near-edge structure evidence for quadrivalent nickel in nickel battery electrodes. *J. Electrochem. Soc.* 143, 1613–1617.
86. Chebiam, R., Prado, F., and Manthiram, A. (2001). Soft chemistry synthesis and characterization of layered $\text{Li}_{1-x}\text{Ni}_{1-y}\text{Co}_y\text{O}_{2-\delta}$ ($0 \leq x \leq 1$ and $0 \leq y \leq 1$). *Chem. Mater.* 13, 2951–2957.
87. Dean, J.A. (1990). Lange's handbook of chemistry. *Mater. Manufacturing Process* 5, 687–688.
88. Li, K., and Xue, D. (2006). Estimation of electronegativity values of elements in different valence states. *J. Phys. Chem. A* 110, 11332–11337.
89. Hong, W.T., Welsch, R.E., and Shao-Horn, Y. (2015). Descriptors of oxygen-evolution activity for oxides: a statistical evaluation. *J. Phys. Chem. C* 120, 78–86.
90. Sarma, D.D., Shanthi, N., Barman, S.R., Hamada, N., Sawada, H., and Terakura, K. (1995). Band theory for ground-state properties and excitation spectra of perovskite LaMO_3 (M=Mn, Fe, Co, Ni). *Phys. Rev. Lett.* 75, 1126–1129.
91. May, K.J., Carlton, C.E., Stoerzinger, K.A., Risch, M., Suntivich, J., Lee, Y.-L., Grimaud, A., and Shao-Horn, Y. (2012). Influence of oxygen evolution during water oxidation on the surface of perovskite oxide catalysts. *J. Phys. Chem. Lett.* 3, 3264–3270.
92. Risch, M., Grimaud, A., May, K.J., Stoerzinger, K.A., Chen, T.J., Mansour, A.N., and Shao-Horn, Y. (2013). Structural changes of cobalt-based perovskites upon water oxidation investigated by EXAFS. *J. Phys. Chem. C* 117, 8628–8635.
93. Rong, X., Parolin, J., and Kolpak, A.M. (2016). A fundamental relationship between reaction mechanism and stability in metal oxide catalysts for oxygen evolution. *ACS Catal.* 6, 1153–1158.
94. Nishio, K., Molla, S., Okugaki, T., Nakanishi, S., Nitta, I., and Kotani, Y. (2015). Effects of carbon on oxygen reduction and evolution reactions of gas-diffusion air electrodes based on perovskite-type oxides. *J. Power Sourc.* 298, 236–240.
95. Deganello, F., Licta, L.F., Leonardi, S.G., and Neri, G. (2016). Electrochemical properties of Ce-doped SrFeO_3 perovskites-modified electrodes towards hydrogen peroxide oxidation. *Electrochim. Acta* 190, 939–947.
96. Suntivich, J., Hong, W.T., Lee, Y.-L., Rondinelli, J.M., Yang, W., Goodenough, J.B., Dabrowski, B., Freeland, J.W., and Shao-Horn, Y. (2014). Estimating hybridization of transition metal and oxygen states in perovskites from Ok-edge x-ray absorption spectroscopy. *J. Phys. Chem. C* 118, 1856–1863.
97. Freeland, J.W., van Veenendaal, M., and Chakhalian, J. (2016). Evolution of electronic structure across the rare-earth RNiO_3 series. *J. Electron Spectrosc. Relat. Phenomena* 208, 56–62.
98. Han, B., Qian, D., Risch, M., Chen, H., Chi, M., Meng, Y.S., and Shao-Horn, Y. (2015). Role of LiCoO_2 surface terminations in oxygen reduction and evolution kinetics. *J. Phys. Chem. Lett.* 6, 1357–1362.
99. Zhang, M., De Respinis, M., and Frei, H. (2014). Time-resolved observations of water oxidation intermediates on a cobalt oxide nanoparticle catalyst. *Nat. Chem.* 6, 362–367.
100. Gerken, J.B., McAlpin, J.G., Chen, J.Y., Rigsby, M.L., Casey, W.H., Britt, R.D., and Stahl, S.S. (2011). Electrochemical water oxidation with cobalt-based electrocatalysts from pH 0–14: the thermodynamic basis for catalyst structure, stability, and activity. *J. Am. Chem. Soc.* 133, 14431–14442.
101. Jagadale, A.D., Dubal, D.P., and Lokhande, C.D. (2012). Electrochemical behavior of potentiodynamically deposited cobalt oxyhydroxide (CoOOH) thin films for supercapacitor application. *Mater. Res. Bull.* 47, 672–676.
102. Nemudry, A., Goldberg, E.L., Aguirre, M., and Alario-Franco, M.Á. (2002). Electrochemical topotactic oxidation of nonstoichiometric perovskites at ambient temperature. *Solid State Sci.* 4, 677–690.
103. Grenier, J.C., Wattiaux, A., Doumerc, J.P., Dordor, P., Fournes, L., Chaminade, J.P., and Pouchard, M. (1992). Electrochemical oxygen intercalation into oxide networks. *J. Solid State Chem.* 96, 20–30.
104. Yang, M.-R., and Ke, W.-H. (2008). The doping effect on the electrochemical properties of $\text{LiFe}_{0.95}\text{Mn}_{0.05}\text{PO}_4$ (M= Mg^{2+} , Ni^{2+} , Al^{3+} , or V^{3+}) as cathode materials for lithium-ion cells. *J. Electrochem. Soc.* 155, A729–A732.
105. Goodenough, J.B., and Park, K.S. (2013). The Li-ion rechargeable battery: a perspective. *J. Am. Chem. Soc.* 135, 1167–1176.
106. Rossmeisl, J., Qu, Z.-W., Zhu, H., Kroes, G.-J., and Nørskov, J.K. (2007). Electrolysis of water on oxide surfaces. *J. Electroanal. Chem.* 607, 83–89.
107. Man, I.C., Su, H.Y., Calle-Vallejo, F., Hansen, H.A., Martínez, J.I., Inoglu, N.G., Kitchin, J., Jaramillo, T.F., Nørskov, J.K., and Rossmeisl, J. (2011). Universality in oxygen evolution electrocatalysis on oxide surfaces. *ChemCatChem* 3, 1159–1165.
108. Goodenough, J.B., Manoharan, R., and Paranthaman, M. (1990). Surface protonation and electrochemical activity of oxides in aqueous solution. *J. Am. Chem. Soc.* 112, 2076–2082.
109. Nørskov, J.K., Rossmeisl, J., Logadottir, A., Lindqvist, L., Kitchin, J.R., Bligaard, T., and Jonsson, H. (2004). Origin of the overpotential for oxygen reduction at a fuel-cell cathode. *J. Phys. Chem. B* 108, 17886–17892.
110. Nørskov, J.K., Bligaard, T., Rossmeisl, J., and Christensen, C.H. (2009). Towards the computational design of solid catalysts. *Nat. Chem.* 1, 37–46.
111. Koper, M.T. (2011). Thermodynamic theory of multi-electron transfer reactions: implications for electrocatalysis. *J. Electroanal. Chem.* 660, 254–260.
112. Lee, Y.-L., Gadre, M.J., Shao-Horn, Y., and Morgan, D. (2015). Ab initio GGA+U study of oxygen evolution and oxygen reduction electrocatalysis on the (001) surfaces of lanthanum transition metal perovskites LaBO_3 (B= Cr, Mn, Fe, Co and Ni). *Phys. Chem. Chem. Phys.* 17, 21643–21663.
113. Koper, M.T.M. (2013). Theory of multiple proton-electron transfer reactions and its implications for electrocatalysis. *Chem. Sci.* 4, 2710–2723.
114. Kuo, D.Y., Kawasaki, J.K., Nelson, J.N., Kloppenburg, J., Hautier, G., Shen, K.M., Schlom, D.G., and Suntivich, J. (2017). Influence of surface adsorption on the oxygen evolution reaction on $\text{IrO}_2(110)$. *J. Am. Chem. Soc.* 139, 3473–3479.
115. Matsumoto, Y., Yoneyama, H., and Tamura, H. (1977). Influence of the nature of the conduction band of transition metal oxides on catalytic activity for oxygen reduction. *J. Electroanal. Chem. Interfacial Electrochem.* 83, 237–243.
116. Matsumoto, Y., Yoneyama, H., and Tamura, H. (1977). Catalytic activity for electrochemical reduction of oxygen of lanthanum nickel oxide and related oxides. *J. Electroanal. Chem. Interfacial Electrochem.* 79, 319–326.
117. Matumoto, Y., Yoneyama, H., and Tamura, H. (1975). A new catalyst for cathodic reduction of oxygen: lanthanum nickel oxide. *Chem. Lett.* 4, 661–662.
118. Zagal, J.H., and Koper, M. (2016). Reactivity descriptors for the activity of molecular MN4 catalysts for the oxygen reduction reaction. *Angew. Chem. Int. Ed.* 55, 14510–14521.
119. Zagal, J., Paez, M., Tanaka, A., Dos Santos, J., and Linkous, C. (1992). Electrocatalytic activity of metal phthalocyanines for oxygen reduction. *J. Electroanal. Chem.* 339, 13–30.
120. Zhu, H., Zhang, S., Huang, Y.-X., Wu, L., and Sun, S. (2013). Monodisperse $\text{M}_x\text{Fe}_{3-x}\text{O}_4$ (M= Fe, Cu, Co, Mn) nanoparticles and their electrocatalysis for oxygen reduction reaction. *Nano Lett.* 13, 2947–2951.
121. Wei, C., Feng, Z., Scherer, G.G., Barber, J., Shao-Horn, Y., and Xu, Z.J. (2017). Cations in octahedral sites: a descriptor for oxygen electrocatalysis on transition-metal spinels. *Adv. Mater.* 29, <https://doi.org/10.1002/adma.201606800>.
122. Friebel, D., Louie, M.W., Bajdich, M., Sanwald, K.E., Cai, Y., Wise, A.M., Cheng, M.J., Sokaras, D., Weng, T.C., Alonso-Mori, R., et al. (2015). Identification of highly active Fe sites in (Ni/Fe) OOH for electrocatalytic water splitting. *J. Am. Chem. Soc.* 137, 1305–1313.
123. Li, N., Bediako, D.K., Hadt, R.G., Hayes, D., Kempa, T.J., von Cube, F., Bell, D.C., Chen, L.X., and Nocera, D.G. (2017). Influence of iron doping on tetravalent nickel content in catalytic oxygen evolving films. *Proc. Natl. Acad. Sci. USA* 114, 1486–1491.
124. Görlin, M., Ferreira de Araújo, J., Schmies, H., Bernsmeyer, D., Dresp, S.r., Gleich, M., Jusys,

- Z., Chernev, P., Krahnert, R., and Dau, H. (2017). Tracking catalyst redox states and reaction dynamics in Ni-Fe oxyhydroxide oxygen evolution reaction electrocatalysts: the role of catalyst support and electrolyte pH. *J. Am. Chem. Soc.* 139, 2070–2082.
125. Grimaud, A., Demortiere, A., Saubanere, M., Dachraoui, W., Duchamp, M., Doublet, M.-L., and Tarascon, J.-M. (2016). Activation of surface oxygen sites on an iridium-based model catalyst for the oxygen evolution reaction. *Nat. Energ.* 2, 16189.
126. Bing, Y., Liu, H., Zhang, L., Ghosh, D., and Zhang, J. (2010). Nanostructured Pt-alloy electrocatalysts for PEM fuel cell oxygen reduction reaction. *Chem. Soc. Rev.* 39, 2184–2202.
127. Ahn, H.S., and Bard, A.J. (2016). Surface Interrogation scanning electrochemical microscopy of $\text{Ni}_{1-x}\text{Fe}_x\text{OOH}$ ($0 < x < 0.27$) oxygen evolving catalyst: kinetics of the “fast” iron sites. *J. Am. Chem. Soc.* 138, 313–318.
128. Klaus, S., Cai, Y., Louie, M.W., Trotochaud, L., and Bell, A.T. (2015). Effects of Fe electrolyte impurities on $\text{Ni}(\text{OH})_2/\text{NiOOH}$ structure and oxygen evolution activity. *J. Phys. Chem. C* 119, 7243–7254.
129. Stevens, M.B., Trang, C.D., Enman, L.J., Deng, J., and Boettcher, S.W. (2017). Reactive Fe-sites in Ni/Fe (oxy) hydroxide are responsible for exceptional oxygen electrocatalysis activity. *J. Am. Chem. Soc.* 139, 11361–11364.
130. Burke, M.S., Enman, L.J., Batchellor, A.S., Zou, S., and Boettcher, S.W. (2015). Oxygen evolution reaction electrocatalysis on transition metal oxides and (oxy) hydroxides: activity trends and design principles. *Chem. Mater.* 27, 7549–7558.
131. Zhou, D., Cai, Z., Bi, Y., Tian, W., Luo, M., Zhang, Q., Zhang, Q., Xie, Q., Wang, J., Li, Y., et al. (2017). Effects of redox-active interlayer anions on the oxygen evolution reactivity of NiFe-layered double hydroxide nanosheets. *Nano Res.* <https://doi.org/10.1007/s12274-017-1750-9>.
132. Stoerzinger, K.A., Rao, R.R., Wang, X.R., Hong, W.T., Rouleau, C.M., and Shao-Horn, Y. (2017). The role of Ru redox in pH-dependent oxygen evolution on rutile ruthenium dioxide surfaces. *Chem* 2, 668–675.
133. Stoerzinger, K.A., Qiao, L., Biegalski, M.D., and Shao-Horn, Y. (2014). Orientation-dependent oxygen evolution activities of rutile IrO_2 and RuO_2 . *J. Phys. Chem. Lett.* 5, 1636–1641.
134. Godwin, I.J., Doyle, R.L., and Lyons, M.E. (2014). The mechanism of oxygen reactions at porous oxide electrodes III. Water oxidation catalysis at RuO_2/NiO mixed oxide electrodes. *J. Electrochem. Soc.* 161, F906–F917.
135. Lyons, M.E., and Floquet, S. (2011). Mechanism of oxygen reactions at porous oxide electrodes. Part 2—oxygen evolution at RuO_2 , IrO_2 and $\text{Ir}_x\text{Ru}_{1-x}\text{O}_2$ electrodes in aqueous acid and alkaline solution. *Phys. Chem. Chem. Phys.* 13, 5314–5335.
136. Ping, Y., Nielsen, R.J., and Goddard, W.A., III (2016). The reaction mechanism with free energy barriers at constant potentials for the oxygen evolution reaction at the $\text{IrO}_2(110)$ surface. *J. Am. Chem. Soc.* 139, 149–155.
137. Shannon, R.D. (1976). Revised effective ionic radii and systematic studies of interatomic distances in halides and chalcogenides. *Acta Cryst. A* 32, 17.